Archive of Applied Mechanics (2024) 94:3071–3099
https://doi.org/10.1007/s00419-024-02658-7

ORIGINAL

Abdullah H. Sofiyev

Modeling and solution of eigenvalue problems of laminated cylindrical shells consisting of nanocomposite plies in thermal environments

Received: 23 April 2024 / Accepted: 10 July 2024 / Published online: 23 July 2024

Abstract This work is dedicated to the modeling and solution of eigenvalue problems within shear deformation theory (SDT) of laminated cylindrical shells containing nanocomposite plies subjected to axial compressive load in thermal environments. In this study, the shear deformation theory for homogeneous laminated shells is extended to laminated shells consisting of functionally graded (FG) nanocomposite layers. The nanocomposite plies of laminated cylindrical shells (LCSs) are arranged in a piecewise FG distribution along the thickness direction. Temperature-dependent material properties of FG-nanocomposite plies are estimated through a micromechanical model, and CNT efficiency parameters are calibrated based on polymer material properties obtained from molecular dynamics simulations. After mathematical modeling, second-order time-dependent and fourth-order coordinate-dependent partial differential equations are derived within SDT, and a closed-form solution for the dimensionless frequency parameter and critical axial load is obtained for first time. After the accuracy of the applied methodology is confirmed by numerical comparisons, the unique influences of ply models, the number and sequence of plies and the temperature on the critical axial load and vibration frequency parameter within SDT and Kirchhoff–Love theory (KLT) are presented with numerical examples.

Keywords Laminated cylindrical shells · Nanocomposite plies · Thermal effect · Axial critical load · Frequency parameter · Shear deformation theory

1 Introduction

Since polymers have been frequently used in different areas of technology and our daily life in the last century, their chemical, physical and mechanical properties have been examined in detail in different environments and workers. Starting from the beginning of the twenty-first century, nanomaterials, the latest achievement of material science, began to be used to further improve the functionality of polymers and expand their applications [1]. The unique structure of carbon nanotubes (CNTs) and their extraordinary mechanical, electrical, optical and thermal properties have been proven theoretically and experimentally, enabling them to be used as main structural elements as well as reinforcement elements [2–4]. While CNTs typically provide high mechanical strength, electrical conductivity and thermal stability, polymers are tunable structures and can be easily produced by a solution or melting process at low costs, keeping CNT/polymer composites, which are their mixtures, always on the agenda. The synthesis, structure, properties and possible applications of CNT/polymer

A. H. Sofiyev (✉)
Department of Mathematics, Istanbul Ticaret University, Beyoglu 34445, Istanbul, Turkey
e-mail: aavey@ticaret.edu.tr

A. H. Sofiyev
Scientific Research Department, Azerbaijan University of Architecture and Construction, Baku 1073, Azerbaijan

A. H. Sofiyev
Scientific Research Center of Baku Engineering University, Baku AZ0101, Azerbaijan

materials are extensively investigated in both academia and industry [5–7]. CNT/polymer nanocomposites are also widely used in the aerospace industry and defense industry, where lightness, high strength and resistance to high temperatures and energy are required, as well as high conductivity, strength and thermal stability [8, 9]. The use of nanocomposites as different structural elements in industries requiring advanced technology should be based on serious mathematical modeling to examine their behavior. The literature review presented above clearly shows that the stability and vibration issues of FG-nanocomposite cylindrical shells subjected to axial load in thermal environments have received limited attention yet in the framework of SDT. In fact, it is known that the first studies on the stability of layered nanocomposite cylindrical shells were proposed by Shen and co-authors [10–13]. However, in those studies, graphene-reinforced composite (GRC) layered cylindrical shells, whose layers consist of isotropic material, are used. Additionally, in those studies, the nonlinear stability problem of GRC layered cylindrical shells subjected to different individual loads such as axial, lateral and torsional loads is solved numerically using the Galerkin approach, followed by the singular perturbation technique with the two-stage perturbation approach. Following these studies, Ninh and his colleagues examined the dynamic behavior of GRC layered structural elements resting on the various elastic foundations using different theories [14–17]. Among the studies on the stability and vibration behavior of laminated structural elements consisting of FG-nanocomposite layers with orthotropic properties, the studies of Liew et al. [18, 19] can be shown as one of the first studies. In those studies, the vibrations of laminated plates and cylindrical panels consisting of FG-nanocomposite layers were solved numerically using the Galerkin approach and the element-free kp-Ritz method. Duc et al. [20] proposed an analytical and finite element approach for the buckling problem of laminated FG-nanocomposite plates. Chakraborty et al. [21] presented stability and vibration analysis of FG-nanocomposite laminated cylindrical shell panels using semi-analytical approach.

In this study, the shear deformation theory proposed by Ambartsumyan [22] is extended to laminated cylindrical shells, the basic relations and governing equations are modified, and the closed-form solution based on new relations and equations are proposed. Following this trend, research in this field continues, although it is sparse. Among them, Avey et al. [23, 24] analyzed the vibration of shallow shell and thermal buckling of conical shells composed of laminated FG-nanocomposite plies within SDT. Shen et al. [25] examined buckling behaviors of axially loaded laminated cylindrical shells made of FG-nanocomposite plies in the thermal environments using the asymptotic sense by means of a singular perturbation technique in associate with a two-step perturbation approach.

The organization of the present work is as follows: in Sect. 2, the basic partial differential equations valid for the stability and vibration of laminated cylindrical shells consisting of nanocomposite plies subjected to axial compressive loading are determined. In Sects. 3 and 4, basic partial differential equations are transformed into ordinary differential equations by the Galerkin method and a closed-form solution for vibration frequency and critical axial load within SDT is obtained. The proposed approach is validated and applied in a large systematic study in Sect. 5, the results of which are summarized in Sect. 6.

2 Multiscale modeling of laminated nanocomposite cylindrical shells under axial load

As shown in Fig. 1, a laminated cylindrical shell containing N nanocomposite plies with length L, average radius R and total thickness h is considered. It is assumed that the plies are perfectly and rigidly bonded to each other and that the plies do not break away from each other when a deformation occurs. The cylindrical shell consisting of N plies have the piecewise continuous FG model, and each ply consists of CNT-reinforced polymer matrix and has the same CNT volume fraction. The cylindrical shell has curvilinear coordinates (x, y, z) where x is in the axial direction, y is in the circumferential direction, and z is in the inward normal direction to the reference surface. The origin of the coordinate system is located on the reference surface of the cylinder and is selected at its left end. Three perpendicular displacements of any point on the reference surface are represented as U, V and W, respectively.

The Airy stress function, Φ, provides the following relations:

$$(N_{11},\ N_{22},\ N_{12}) = \left(h\frac{\partial^2\Phi}{\partial y^2},\ h\frac{\partial^2\Phi}{\partial x^2},\ -h\frac{\partial^2\Phi}{\partial x\partial y}\right) \tag{1}$$

The pre-buckling properties of the laminated nanocomposite cylindrical shells can be expressed as follows, denoted by the superscript "0" [26–29]:

$$N_{11}^0 = -N_{\mathrm{ax}},\quad N_{22}^0 = N_{12}^0 = 0 \tag{2}$$

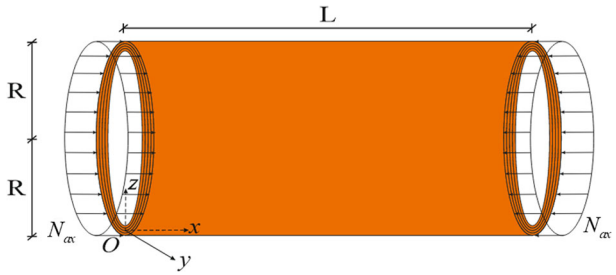

Fig. 1 Laminated cylindrical shell under an axial load and coordinate system

where N_{ij}^0 are the membrane forces for the condition with zero initial moments and N_{ax} is an axial load.

To extend shear deformation theory of the Ambartsumyan to the functionally graded nanocomposite shells, equivalent material properties need to be estimated to account for the influence of CNTs. For this purpose, multiscale modeling of CNTs and matrix is performed in the study. It is known that the effective material properties of nanocomposites largely depend on the structure of CNTs [6, 7, 30–33]. To predict the effective material properties forming the plies of laminated nanocomposite cylindrical shells, the extended Voigt model (mixture rule) is used, where the CNT efficiency parameters are defined to account for the size dependence of the resulting nanostructures [33–35].

According to this rule, the effective Young's modulus and shear modulus of each ply can be estimated as follows [18, 21, 23, 24]:

$$\begin{aligned} &Y_{11(z_1,\text{T})}^{(k)} = \eta_1^{(k)} V_{\text{cn}}^{(k)} Y_{11\text{T}}^{\text{cn}(k)} + V_{\text{p}}^{(k)} Y_{\text{pT}}^{(k)}, \quad \frac{\eta_2^{(k)}}{Y_{22(z_1,\text{T})}^{(k)}} = \frac{V_{\text{cn}}^{(k)}}{Y_{22\text{T}}^{\text{cn}(k)}} + \frac{V_p^{(k)}}{Y_{\text{pT}}^{(k)}}, \quad \frac{\eta_3^{(k)}}{G_{12(z_1,\text{T})}^{(k)}} = \frac{V_{\text{cn}}^{(k)}}{G_{12\text{T}}^{\text{cn}(k)}} + \frac{V_{\text{p}}^{(k)}}{G_{\text{pT}}^{(k)}}, \\ &G_{13(z_1,\text{T})}^{(k)} = G_{12(z_1,\text{T})}^{(k)}, \quad G_{23(z_1,\text{T})}^{(k)} = 1.2 G_{12(z_1,\text{T})}^{(k)} \end{aligned} \tag{3}$$

where $Y_{iiT}^{\text{cn}(k)}$, $G_{ijT}^{\text{cn}(k)} (i = 1, 2, j = 1, 2, 3)$ and $Y_{\text{pT}}^{(k)}$, $G_{\text{pT}}^{(k)}$ are the Young and shear moduli of the CNT and polymer, respectively, in the kth-ply, $V_{\text{cn}}^{(k)}$ and $V_{\text{p}}^{(k)}$ represent the volume fractions of CNTs and polymer matrix in the kth-ply, respectively, and they are related by the equation $V_{\text{cn}}^{(k)} + V_{\text{p}}^{(k)} = 1$. To account for the small-scale influence, the efficiency parameters of CNT denoted by symbols $\eta_j^{(k)} (j = 1, 2, 3)$ are obtained by matching the Young's moduli of the nanocomposite-ply predicted from the extended Voight models to those from the MD simulations, as previously reported in Ref. [35].

Temperature-dependent material properties are also considered in the current study, and thermal expansion coefficients of nanocomposite-ply in the longitudinal and transverse directions are defined as [36–39]:

$$\begin{aligned} \alpha_{11(z_1,\text{T})}^{(k)} &= \frac{V_{\text{cn}}^{(k)} Y_{11\text{T}}^{\text{cn}(k)} \alpha_{11\text{T}}^{\text{cn}(k)} + V_{\text{p}}^{(k)} Y_{\text{pT}}^{(k)} \alpha_{\text{T}}^{p(k)}}{V_{cn}^{(k)} Y_{11T}^{cn(k)} + V_p^{(k)} Y_{pT}^{(k)}}, \\ \alpha_{22(z_1,\text{T})}^{(k)} &= \left(1 + \nu_{12}^{\text{cn}(k)}\right) V_c^{(k)} \alpha_{22\text{T}}^{\text{cn}(k)} + \left(1 + \nu_{\text{p}}^{(k)}\right) V_{\text{p}}^{(k)} \alpha_{\text{pT}}^{(k)} - \nu_{12}^{(k)} \alpha_{11(z_1,\text{T})}^{(k)} \end{aligned} \tag{4}$$

where, $\alpha_{ii\text{T}}^{\text{cn}(k)}$ and $\alpha_{\text{pT}}^{(k)}$ are the thermal expansion coefficients of CNTs and the polymer in the kth-ply, respectively.

Since the Poisson ratio and mass density of the nanocomposite layer vary within a small range, the Poisson ratio and mass density of the components can be easily expressed according to the conventional mixing rule as:

$$\nu_{12}^{(k)} = V_{\text{cn}}^{*(k)} \nu_{12}^{\text{cn}(k)} + V_{\text{p}}^{(k)} \nu^{p(i)}, \quad \rho_{\text{t}}^{(k)} = V_{\text{cn}}^{*(k)} \rho_{\text{cn}}^{(k)} + V_{\text{p}}^{(k)} \rho_{\text{p}}^{(k)} \tag{5}$$

The mathematical laws which characterize the CNT volume fraction distributions in the kth-ply are given as follows [36]:

$$V_{\text{cn}}^{(k)} = V_{\text{cn}}^{*(k)} \quad (U) \tag{6a}$$

$$V_{\text{cn}}^{(k)} = 2(0.5 - z_1) V_{\text{cn}}^{*(k)} \quad (V) \tag{6b}$$

Fig. 2 The patterns in the layers **a** (U), **b** (◊), **c** (V) and **d** (X)

$$V_{\mathrm{cn}}^{(k)} = 2(1-2|z_1|)V_{\mathrm{cn}}^{*(k)} \quad (\diamond) \tag{6c}$$

$$V_{\mathrm{cn}}^{(k)} = 4|z_1|V_{\mathrm{cn}}^{*(k)} \quad (X) \tag{6d}$$

where

$$\frac{1}{V_{\mathrm{cn}}^{*(k)}} = \frac{\rho_{\mathrm{cn}}^{(k)}}{m_{\mathrm{cn}}^{(k)}\rho_{\mathrm{p}}^{(k)}} - \frac{\rho_{\mathrm{cn}}^{(k)}}{\rho_{\mathrm{p}}^{(k)}} + 1 \tag{7}$$

in which $m_{\mathrm{cn}}^{(k)}$ denotes the mass fraction of CNTs, $\rho_{\mathrm{cn}}^{(k)}$ and $\rho_{\mathrm{p}}^{(k)}$ are densities of CNTs and matrix phase in the kth-ply, respectively. The models in the plies are modeled as $(\diamond)$, (V), (X) and (U) according to their shape similarities (see Fig. 2):

3 Governing equations

The basic relationships of laminated cylindrical shells consisting of nanocomposite plies with thermoelastic material properties within SDT are defined as follows: [23, 36, 37]:

$$\begin{bmatrix} \tau_{11}^{(k)} \\ \tau_{22}^{(k)} \\ \tau_{12}^{(k)} \end{bmatrix} = \begin{bmatrix} Q_{11(z_1,T)}^{(k)} & Q_{12(z_1,T)}^{(k)} & 0 \\ Q_{21(z_1,T)}^{(k)} & Q_{22(z_1,T)}^{(k)} & 0 \\ 0 & 0 & Q_{66(z_1,T)}^{(k)} \end{bmatrix} \begin{bmatrix} \varepsilon_{11} \\ \varepsilon_{22} \\ \gamma_{12} \end{bmatrix} - \begin{bmatrix} \tau_{11T}^{(k)} \\ \tau_{22T}^{(k)} \\ 0 \end{bmatrix} \tag{8}$$

$$\begin{bmatrix} \tau_{13}^{(k)} \\ \tau_{23}^{(k)} \end{bmatrix} = \begin{bmatrix} Q_{55(z_1,T)}^{(k)} & 0 \\ 0 & Q_{44(z_1,T)}^{(k)} \end{bmatrix} \begin{bmatrix} \gamma_{13} \\ \gamma_{23} \end{bmatrix} \tag{9}$$

$$\tau_{11\mathrm{T}}^{(k)} = \begin{bmatrix} Q_{11(z_1,\mathrm{T})}^{(k)} & 0 \\ 0 & Q_{12(z_1,\mathrm{T})}^{(k)} \end{bmatrix} \begin{bmatrix} \alpha_{11(z_1,\mathrm{T})}^{(k)} \\ \alpha_{22(z_1,\mathrm{T})}^{(k)} \end{bmatrix} (T-T_0), \tau_{22\mathrm{T}}^{(k)} = \begin{bmatrix} Q_{21(z_1,\mathrm{T})}^{(k)} & 0 \\ 0 & Q_{22(\bar{z},\mathrm{T})}^{(k)} \end{bmatrix} \begin{bmatrix} \alpha_{11(z_1,\mathrm{T})}^{(k)} \\ \alpha_{22(z_1,\mathrm{T})}^{(k)} \end{bmatrix} (T-T_0) \tag{10}$$

where $\tau_{ij}^{(k)}$ and $\tau_{ii\mathrm{T}}^{(k)}$ are the stresses and thermal stresses in the $\tau_{ii\mathrm{T}}^{(k)}$-ply, ε_{ii}, γ_{ij} are the strains, $T-T_0=\Delta T$ is the temperature change, at the reference temperature T_0 the thermal strains are absent and the elements of elastic constant tensor $Q_{ij}^{(k)}$ are given by:

$$\begin{aligned} &Q_{11(z_1,\mathrm{T})}^{(k)} = \frac{Y_{11(z_1,\mathrm{T})}^{(k)}}{1-\nu_{12}^{(k)}\nu_{21}^{(k)}}, \quad Q_{22(z_1,\mathrm{T})}^{(k)} = \frac{Y_{22(z_1,\mathrm{T})}^{(k)}}{1-\nu_{12}^{(k)}\nu_{21}^{(k)}}, \quad Q_{12(z_1,\mathrm{T})}^{(k)} = \nu_{21}^{(k)}Q_{11(z_1,\mathrm{T})}^{(k)} = \nu_{12(z_1,\mathrm{T})}^{(k)}Q_{22(z_1,\mathrm{T})}^{(k)} = Q_{21(z_1,\mathrm{T})}^{(k)}, \\ &Q_{44(z_1,\mathrm{T})}^{(k)} = G_{23(z_1,\mathrm{T})}^{(k)}, \quad Q_{55(z_1,\mathrm{T})}^{(k)} = G_{13(z_1,\mathrm{T})}^{(k)}, \quad Q_{66(z_1,\mathrm{T})}^{(k)} = G_{12(z_1,\mathrm{T})}^{(k)}. \end{aligned} \tag{11}$$

in which $-\frac{h}{2}+\frac{h(k-1)}{N} \le z \le -\frac{h}{2}+\frac{hk}{N}$.

Unlike other theories, the SDT of the Ambartsumyan is based on the following assumptions [28].

(a) The displacement u_z normal to the middle surface in each ply is independent of z coordinate.
(b) The shear stress $\tau_{13}^{(k)}$ and $\tau_{23}^{(k)}$ or the corresponding strains $\gamma_{13}^{(k)}$ and $\gamma_{23}^{(k)}$ change according to a given law with respect to the thickness of each ply.
(c) The effect of normal stress $\tau_{33}^{(k)}$ is disregarded during the determination of the displacements $u^{(k)}$ and $v^{(k)}$ as well as in determining stresses $\tau_{11}^{(k)}$ and $\tau_{22}^{(k)}$.

One the basis of assumptions (a) and (b) for the kth-ply, it is assumed that approximately:

$$\varepsilon_{33}^{(k)} = \frac{\partial u_3^{(k)}}{\partial z} =, \quad u_3^{(k)} = u_3^{(k)}(x, y, t) = w(x, y, t) \tag{12}$$

$$\tau_{33}^{(k)} = 0, \quad \tau_{13}^{(k)} = \frac{\mathrm{d}f_1^{(k)}}{\mathrm{d}z}\varphi_1(x, y, t), \quad \tau_{23}^{(k)} = \frac{\mathrm{d}f_2^{(k)}}{\mathrm{d}z}\varphi_2(x, y, t). \tag{13}$$

where $\varphi_i(x,\ y,\ t)$ represent the rotation of the normal to mid-surface about y and x axes, $f^{(k)}(z)$ represents the shape functions that determine the distribution of transverse shear deformations and stresses throughout the thickness in the kth-ply and is a parabolic function.

By using Eqs. (8)–(10), (12) and (13) together, the strains within SDT based on the extended theory can be written as follows [23, 28]:

$$\begin{bmatrix} \varepsilon_{11} \\ \varepsilon_{12} \\ \gamma_{12} \end{bmatrix} = \begin{bmatrix} \varepsilon_{11}^0 - z\frac{\partial^2 w}{\partial x^2} + \Lambda_{1(z,T)}^{(k)}\frac{\partial \varphi_1}{\partial x} \\ \varepsilon_{22}^0 - z\frac{\partial^2 w}{\partial y^2} + \Lambda_{2(z,T)}^{(k)}\frac{\partial \varphi_2}{\partial y} \\ \gamma_{12}^0 - 2z\frac{\partial^2 w}{\partial x \partial y} + \Lambda_{1(z,T)}^{(k)}\frac{\partial \varphi_1}{\partial y} + \Lambda_{2(z,T)}^{(k)}\frac{\partial \varphi_2}{\partial x} \end{bmatrix} \tag{14}$$

where $\varepsilon_{11}^0,\ \varepsilon_{22}^0,\ \gamma_{12}^0$ are the strain components on the reference surface and $\Lambda_{i(z,T)}^{(k)}$ are defined by

$$\Lambda_{1(z,T)}^{(k)} = \int_0^z \frac{1}{Q_{55(z_1,T)}^{(k)}}\frac{\mathrm{d}f^{(k)}}{\mathrm{d}z}\mathrm{d}z, \quad \Lambda_{2(z,T)}^{(k)} = \int_0^z \frac{1}{Q_{44(z_1,T)}^{(k)}}\frac{\mathrm{d}f^{(k)}}{\mathrm{d}z}\mathrm{d}z. \tag{15}$$

The force and moment components can be expressed as follows with the help of stress field components within SDT assumptions [25–29]:

$$\left[N_{ij},\ Q_i,\ M_{ij}\right] = \sum_{k=1}^{N}\int_{z_{k-1}}^{z_k}\left[\sigma_{ij}^{(k)},\ \sigma_{i3}^{(k)},\ z\sigma_{ij}^{(k)}\right]\mathrm{d}z. \tag{16}$$

The thermal forces and moments $(N_{ii}^T,\ M_{ii}^T)$ caused by elevated temperature are defined by [24, 36, 37]:

$$\begin{aligned} \left(N_{11}^T, M_{11}^T\right) &= \sum_{k=1}^{N}\int_{z_{i-1}}^{z_i}\begin{bmatrix} Q_{11(z_1,T)}^{(k)} & 0 \\ 0 & Q_{12(z_1,T)}^{(k)} \end{bmatrix}\begin{bmatrix} \alpha_{11(z_1,T)}^{(k)} \\ \alpha_{22(z_1,T)}^{(k)} \end{bmatrix}(1, z)(T - T_0)\mathrm{d}z, \\ \left(N_{22}^T,\ M_{22}^T\right) &= \sum_{k=1}^{N}\int_{z_{k-1}}^{z_k}\begin{bmatrix} Q_{21(z_1,T)}^{(k)} & 0 \\ 0 & Q_{22(z_1,T)}^{(k)} \end{bmatrix}\begin{bmatrix} \alpha_{11(z_1,T)}^{(k)} \\ \alpha_{22(z_1,T)}^{(k)} \end{bmatrix}(1, z)(T - T_0)\mathrm{d}z. \end{aligned} \tag{17}$$

The dynamic stability equations of laminated cylindrical shells subjected to the axial load can be defined as follows [27]:

$$\begin{aligned} &\frac{\partial M_{11}}{\partial x} + \frac{\partial M_{12}}{\partial y} - Q_1 = 0, \qquad \frac{\partial M_{21}}{\partial x} + \frac{\partial M_{22}}{\partial y} - Q_2 = 0, \\ &\frac{\partial^2 \varepsilon_{11}^0}{\partial y^2} + \frac{\partial^2 \varepsilon_{22}^0}{\partial x^2} - \frac{\partial^2 \gamma_{12}^0}{\partial x^2} + \frac{1}{R}\frac{\partial^2 w}{\partial x^2} = 0, \quad \frac{\partial Q_1}{\partial x} + \frac{\partial Q_2}{\partial y} + \frac{N_y}{R} - N_{\mathrm{ax}}\frac{\partial^2 w}{\partial x^2} = \rho_1\frac{\partial^2 w}{\partial t^2}. \end{aligned} \tag{18}$$

where $\rho_1 = \sum_{k=1}^{N}\int_{z_{k-1}}^{z_k}\rho_t^{(k)}\mathrm{d}z$.

By combining Eqs. (8)-(10), (14), (16) and (18) including thermal effects (17), the dynamic stability equations of laminated cylindrical shells made of nanocomposite-plies under axial load is obtained as follows:

$$\begin{bmatrix} L_{11} & L_{12} & L_{13} & L_{14} \\ L_{21} & L_{22} & L_{23} & L_{24} \\ L_{31} & L_{32} & L_{33} & L_{34} \\ L_{41} & L_{42} & L_{43} & L_{44} \end{bmatrix}\begin{bmatrix} \Phi \\ w \\ \varphi_1 \\ \varphi_2 \end{bmatrix} = \begin{bmatrix} 0 \\ 0 \\ 0 \\ 0 \end{bmatrix} \tag{19}$$

where L_{ij} are differential operators and defined in Appendix A.

4 Solution procedure

The two ends of the laminated cylindrical shell consisting of nanocomposite-pies are subject to simply supported boundary conditions and are mathematically expressed as [36]:

$$\text{At } x = 0,\ L \quad w = \frac{\partial^2 \Phi}{\partial y^2} = \varphi_2 = M_{11} = 0 \tag{20}$$

where the closed or periodicity condition is expressed as

$$\int_0^{2\pi R} \frac{\partial v}{\partial y} \mathrm{d}y = 0 \tag{21}$$

The solution of the set of Eqs. (19) under boundary conditions (20) is sought as follows [27, 28]:

$$\begin{aligned} &\Phi = \overline{\Phi}(t) \sin\left(\frac{m\pi}{L}x\right) \sin\left(\frac{n}{R}y\right) \cos \Omega t, \quad w = \overline{w}(t) \sin\left(\frac{m\pi}{L}x\right) \sin\left(\frac{n}{R}y\right) \cos \Omega t, \\ &\varphi_1 = \overline{\varphi}_1(t) \cos\left(\frac{m\pi}{L}x\right) \sin\left(\frac{n}{R}y\right) \cos \Omega t, \quad \varphi_2 = \overline{\varphi}_2(t) \sin\left(\frac{m\pi}{L}x\right) \cos\left(\frac{n}{R}y\right) \cos \Omega t. \end{aligned} \tag{22}$$

where $\overline{\Phi}(t)$, $\overline{w}(t)$, $\overline{\varphi}_1(t)$, $\overline{\varphi}_2(t)$ are unknown time-dependent parameters, Ω is the frequency and (m, n) are the wave modes.

Applying the Galerkin procedure, incorporating (22) into Eq. (19) and taking into account (2), the non-trivial solution of the resulting system of matrix equations is found by setting the determinant of the characteristic matrix equal to zero:

$$\begin{vmatrix} S_{11} & -S_{12} & S_{13} & S_{14} \\ S_{21} & -S_{22} & S_{23} & S_{24} \\ S_{31} & -S_{32} & S_{33} & S_{34} \\ S_{41} & S_{42} & S_{43} & S_{44} \end{vmatrix} = 0 \tag{23}$$

where $S_{42} = N_{\mathrm{ax}}\left(\frac{m\pi}{L}\right)^2 - \rho_1 \Omega^2$ and other S_{ij} are given in Appendix B.

At $\Omega = 0$, solving Eq. (23), we obtain an expression for the non-dimensional critical axial load:

$$N_{1\mathrm{ax}}^{\mathrm{crst}} = \frac{N_{\mathrm{ax}}^{\mathrm{crst}}}{Y_{\mathrm{pT}_0}^{(k)} h} \tag{24}$$

where $Y_{\mathrm{pT}_0}^{(k)}$ is the Young modulus of polymer in the kth-ply at $T_0 = 300\,(\mathrm{K})$ (at room temperature) and $N_{\mathrm{ax}}^{\mathrm{crst}}$ is the critical axial load of laminated cylindrical shells consisting of nanocomposite-plies in thermal environments based on the SDT and defined as

$$N_{\mathrm{ax}}^{\mathrm{crst}} = \frac{L^2}{m^2\pi^2} \frac{S_{41}P_1 + S_{43}P_3 + S_{44}P_4}{P_2} \tag{25}$$

in which P_i are defined by

$$P_1 = -\begin{vmatrix} S_{12} & S_{13} & S_{14} \\ S_{22} & S_{23} & S_{24} \\ S_{32} & S_{33} & S_{34} \end{vmatrix}, P_2 = \begin{vmatrix} S_{11} & S_{13} & S_{14} \\ S_{21} & S_{23} & S_{24} \\ S_{31} & S_{33} & S_{34} \end{vmatrix}, P_3 = -\begin{vmatrix} S_{11} & S_{12} & S_{14} \\ S_{21} & S_{22} & S_{24} \\ S_{31} & S_{32} & S_{34} \end{vmatrix}, P_4 = \begin{vmatrix} S_{11} & S_{12} & S_{13} \\ S_{21} & S_{22} & S_{23} \\ S_{31} & S_{32} & S_{33} \end{vmatrix} \tag{26}$$

As $N_{\mathrm{ax}} = 0$, solving Eq. (23), we obtain an expression for the non-dimensional frequency parameter of laminated cylindrical shells consisting of nanocomposite-plies in thermal environments based on the SDT:

$$\Omega_1^{\mathrm{st}} = \Omega^{\mathrm{st}} \frac{L^2}{h} \sqrt{\frac{\rho_p^{(k)}}{Y_{\mathrm{pT}_0}^{(k)}}} \tag{27}$$

Table 1 Temperature-dependent material properties for (10, 10) SWCNT

(in K)	(in TPa)			(in 1/K)	
Temperature	$Y_{11\mathrm{T}}^{\mathrm{cn}(k)}$	$Y_{22\mathrm{T}}^{\mathrm{cn}(k)}$	$G_{12\mathrm{T}}^{\mathrm{cn}(k)}$	$\alpha_{11\mathrm{T}}^{\mathrm{cn}(k)}/10^6$	$\alpha_{22\mathrm{T}}^{\mathrm{cn}(k)}/10^6$
300	5.6465	7.0800	1.9445	3.4584	5.1641
500	5.5308	6.9348	1.9643	4.5361	5.0120
700	5.4744	6.8641	1.9644	4.6677	4.8846

where Ω^{st} is the frequency of laminated cylindrical shells consisting of nanocomposite-plies in thermal environments within SDT and expressed by

$$\Omega^{\mathrm{st}} = \sqrt{\frac{S_{41}P_1 + S_{43}P_3 + S_{44}P_4}{P_2\rho_1}} \tag{28}$$

The minimum values of the non-dimensional frequency and critical axial load of laminated cylindrical shells consisting of nanocomposite-plies are obtained by minimizing (24) and (27) according to the wave modes. As the transverse shear deformations are removed from the basic relations, the non-dimensional frequency and critical axial load quantities are obtained within K–L theory. When dimensionless frequency and critical axial load values are presented within the framework of K–L theory in the tables and figures presented in the following stages, K–L is written on the top of these symbols, that is, they are shown as $N_{1\mathrm{ax}}^{\mathrm{crkl}}$ and Ω_1^{kl}.

5 Numerical results and discussion

5.1 Material properties in thermal environments

In this section, numerical results are presented for the critical axial load and frequency parameter of the laminated nanocomposite cylinders, whose material properties depend on the temperature. The nanocomposite plies are composed of Poly (methyl methacrylate) matrix called PMMA reinforced with (10, 10) SWCNTs. The material properties of PMMA are assumed to be [37]:

$$Y_{\mathrm{pT}}^{(k)} = (3520 - 3.4 \cdot T)\mathrm{MPa}, \nu_p^{(k)} = 0.34, \quad \alpha_{\mathrm{pT}}^{(k)} = (45 + 0.0225\Delta T) \times 10^{-6}/\mathrm{K} \tag{29}$$

and the elastic and thermal properties of (10,10) SWCNTs are assumed to be:

$$\begin{aligned}
Y_{11\mathrm{T}}^{\mathrm{cn}(k)} &= 6.18387 - 2.86 \times 10^{-3}T + 4.22867 \times 10^{-6}T^2 - 2.2724 \times 10^{-9}T^3 \\
Y_{22\mathrm{T}}^{\mathrm{cn}(k)} &= 7.75348 - 3.58 \times 10^{-3}T + 5.30057 \times 10^{-6}T^2 - 2.84868 \times 10^{-9}T^3 \\
G_{12}^{\mathrm{cn}(k)} &= 1.80126 + 0.77845 \times 10^{-3}T - 1.1279 \times 10^{-6}T^2 + 4.93484 \times 10^{-10}T^3 \\
\alpha_{11\mathrm{T}}^{\mathrm{cn}(k)} &= \left(-1.12148 + 2.289 \times 10^{-2}T - 2.88155 \times 10^{-5}T^2 + 1.13253 \times 10^{-8}T^3\right) \cdot 10^{-6}/K \\
\alpha_{22\mathrm{T}}^{\mathrm{cn}(k)} &= \left(5.43874 - 9.95498 \times 10^{-4}T + 3.13525 \times 10^{-7}T^2 - 3.56332 \times 10^{-12}T^3\right) \cdot 10^{-6}/K
\end{aligned} \tag{30}$$

The material properties of PMMA are $Y_{\mathrm{pT}_0}^{(k)} = 2500\,\mathrm{MPa}$, $\alpha_{\mathrm{pT}_0}^{(k)} = 45 \times 10^{-6}/\mathrm{K}$ for $T_0 = 300\,\mathrm{K}$. The temperature-dependent material properties for (10, 10) SWCNT with a length of 9.26 nm, an average radius of 0.68 nm, and a thickness of 0.067 nm and $\nu_{12}^{\mathrm{cn}(k)} = 0.175$ in the kth-ply for different T are listed in Table 1 using Eq. (30).

The CNT efficient parameters in the kth-ply are defined as:

$$\begin{aligned}
&\eta_1^{(k)} = 0.137, \ \eta_2^{(k)} = 1.022, \ \eta_{13}^{(k)} = 0.715 \text{ for } V_{\mathrm{cn}}^{*(k)} = 0.12 \\
&\eta_1^{(k)} = 0.142, \ \eta_2^{(k)} = 1.626, \ \eta_{13}^{(k)} = 1.138 \text{ for } V_{\mathrm{cn}}^{*(k)} = 0.17 \\
&\eta_1^{(k)} = 0.141, \ \eta_2^{(k)} = 1.585, \ \eta_{13}^{(k)} = 1.109 \text{ for } V_{\mathrm{cn}}^{*(k)} = 0.28
\end{aligned} \tag{31}$$

Table 2 Comparison of dimensionless critical axial load of the single layer nanocomposite cylindrical shell in thermal environments with the results of the Shen [36]

	$\tilde{N}_{\text{ax}}^{\text{crst}}$ (in kPa), $(m_{\text{cr}}, n_{\text{cr}})$ for $V_{cn}^{*(k)} = 0.12$			
	Uniform (U)		Sandglass profile (X)	
Temperature	Z = 100			
T(K)	Ref. [36]	Present study	Ref. [36]	Present study
300	74.46 (1,4)	74.45 (1,4)	87.36 (1,4)	86.99 (1,4)
500	58.69 (1,4)	58.77 (1,4)	70.65 (1,4)	70.77 (1,4)
700	44.33 (1,4)	44.61 (1,4)	55.46 (1,4)	54.72 (1,4)
T(K)	Z = 300			
300	75.85 (2,4)	75.86 (2,4)	89.61 (1,3)	89.19 (1,3)
500	61.09 (2,4)	60.98 (2,4)	67.94 (1,3)	67.63 (1,3)
700	41.95 (1,3)	42.32 (1,3)	46.18 (1,3)	45.99 (1,3)
T(K)	Z = 500			
300	75.17 (2,4)	75.20 (2,4)	86.39 (2,4)	85.82 (2,4)
500	58.35 (2,4)	58.55 (2,4)	68.57 (2,4)	68.54 (2,4)
700	42.53 (2,4)	41.69 (2,4)	47.42 (1,3)	47.64 (1,3)

Table 3 Comparison the non-dimensional frequency parameter ($\overline{\Omega}^{\text{st}}$) for (0°/90°/0°/90°/0°)-array laminated nanocomposite square plates consisting of U and X model plies

	$\overline{\Omega}^{\text{st}}$ for U model		
	$V_{\text{cn}}^{*(k)} = 0.11$	$V_{\text{cn}}^{*(k)} = 0.14$	$V_{\text{cn}}^{*(k)} = 0.17$
Lei et al. [18]	14.277	15.270	17.709
Present study	14.200	14.464	17.007
	$\overline{\Omega}^{st}$ for X model		
Lei et al. [18]	14.383	15.397	17.882
Present study	14.617	15.281	18.083

5.2 Comparative examples

As part of the validation of the current method, the critical axial load of single-layer nanocomposite cylindrical shells in thermal environments in the framework of SDT is compared in Table 2 with the results of the Shen [36], who use the high-order shear deformation shell theory and singular perturbation technique. The mechanical and thermal properties of nanocomposite piles are calculated by the formula (30) and are presented in Table 1 and in the expression (31). In order for us to be able to compare with the results of the Shen [36] , the expression of the critical axial load (25) has been converted to the form used in that study: $\tilde{N}_{\text{ax}}^{\text{crst}} = 2\pi R \cdot N_{\text{ax}}^{\text{crst}}$. Here $(m_{\text{cr}}, n_{\text{cr}})$ are the wave numbers corresponding to the minimum values of the critical axial load. The geometric shell characteristics were taken from the Shen [36] and are as follows: $R/h = 30$, $h = 2$ mm, $Z = L^2/Rh$ and $V_{\text{cn}}^{*(k)} = 0.12$. Here Z is the Batdorf shell parameter. As expected, the results of the Shen [32] are in good agreement with our results.

In the second example, a comparison of the dimensionless frequency parameter ($\overline{\Omega}^{\text{st}}$) with the results of Lei et al. [18] is presented in Table 3 for cross-ply-laminated nanocomposite square plates with (0°/90°/0°/90°/0°)-array within SDT for $L = b = 10h$, $(m, n) = (1, 1)$. Material properties of the matrix layers consisting of PmPV are: $Y_{\text{p}}^{(k)} = 2.1$ GPa, $\nu_{\text{p}}^{(k)} = 0.34$ and $\rho_{\text{p}}^{(k)} = 1150\,\text{kg/m}^3$. The mechanical properties of CNT are: $Y_{11\text{cn}}^{(k)} = 5.6466$ TPa, $Y_{22\text{cn}}^{(k)} = 7.08$ TPa, $G_{12\text{cn}}^{(k)} = 1.9445$ TPa, $\nu_{12\text{cn}}^{(k)} = 0.175$ and $\rho_{\text{cn}}^{(k)} = 1400\,\text{kg/m}^3$. The CNT efficiency parameters in the layers are as follows: $\eta_1^{(k)} = 0.149$, $\eta_2^{(k)} = \eta_3^{(k)} = 0.934$ for $V_{\text{cn}}^{*(k)} = 0.11$, $\eta_1^{(k)} = 0.15$, $\eta_2^{(k)} = \eta_3^{(k)} = 0.941$ for $V_{\text{cn}}^{*(k)} = 0.14$ and $\eta_1^{(k)} = 0.149$, $\eta_2^{(k)} = \eta_3^{(k)} = 1.381$ for $V_{\text{cn}}^{*(k)} = 0.17$. The values of $\overline{\Omega}^{\text{st}}$ for cross-ply-laminated plates consisting of plies with U and X models are compared with the results of the Lei et al. [18], who use the kp-Ritz method in the solution. The $\overline{\Omega}^{\text{st}}$ is calculated using the expression: $\overline{\Omega}^{\text{st}} = \Omega^{\text{st}}\left(L^2/h\right)\sqrt{\rho_{\text{p}}^{(k)}/E_{\text{p}}^{(k)}}$ at $k = 5$. Here, $\overline{\Omega}^{\text{st}}$ is calculated using Eq. (28) at $R \to \infty$. Table 3 also reveals that the $\overline{\Omega}^{\text{st}}$ values of the cross-ply-laminated nanocomposite plate consisting of five piles ($k = 5$) containing U and X model plies are in good agreement.

Table 4 Comparison of the results including the effects of temperature and CNT volume fraction on the $\overline{\Omega}^{\mathrm{st}}$ with the results of Ref. [37]

$V_{\mathrm{cn}}^{*(1)}$	Models	$\overline{\Omega}^{\mathrm{st}}(n=2)$			
		Shen and Xiang [37] $T(\mathrm{K})=300$ K	Present study	Shen and Xiang [37] $T(\mathrm{K})=700$ K	Present study
0.12	U	2.0449	2.0485	1.4322	1.4497
	V	2.0847	2.0890	1.4661	1.4618
	X	2.1253	2.1145	1.5293	1.5122
0.17	U	2.6196	2.6242	1.8951	1.8540
	V	2.6774	2.6838	1.9459	1.8767
	X	2.7457	2.7317	2.0382	1.9470
0.28	U	2.8020	2.8070	1.8568	1.8965
	V	2.8683	2.8857	1.9192	2.0254
	X	3.0480	3.0355	2.1485	2.1724

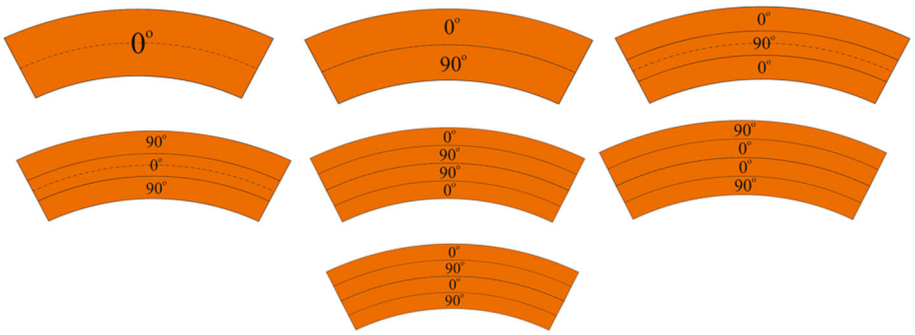

Fig. 3 Cross-sections of single-layer and laminated cylindrical shells consisting of various array plies

In the third example, the comparison of the results including the effects of temperature and CNT volume fraction on the non-dimensional frequency parameter ($\overline{\Omega}^{\mathrm{st}}=\Omega^{\mathrm{st}}\frac{R^2}{h}\sqrt{\frac{\rho_{\mathrm{p}}^{(1)}}{Y_{\mathrm{pT_0}}^{(1)}}}$) for nanocomposite cylindrical shells with the solutions of Ref. [37], who use an improved perturbation technique is presented. The laminated cylindrical shell containing layers with the U, V and X models and for three different volume fractions is reduced to the single-layer cylindrical shell in thermal environments. The expression (28) is used for the calculation of the frequency Ω^{st}, at $Z=L^2/Rh=300$, $R=10h$, $h=5$mm, $T=300$ and 700 K. The values of the $\overline{\Omega}^{\mathrm{st}}$ for single-layer nanocomposite cylinders in thermal environments presented in Table 4 are in very good agreement with the study of the Shen and Xiang [37].

5.3 Parametric studies

In the next stage, numerical examples are conducted and typical results are presented in Tables 5, 6, 7, 8, 9, 10, 11, 12, 13 and 14 and Figs. 3, 4, 5, 6, 7, 8 and 9. For these examples, the total thickness h of laminated nanocomposite cylindrical shells considered is 2.0 mm, the $V_{\mathrm{cn}}^{*(k)}$, L/R and R/h take different values. In numerical examples, six types of laminated nanocomposite cylindrical shells, such as (0°/90°) or LCS2, (0°/90°/0°) or LCS3a, (90°/0°/90°) or LCS3b, (0°/90°/0°/90°) or LCS4a, (0°/90°/90°/0°) or LCS4b and (0°/90°/90°/0°) or LCS3b -plies and single-layer (0°) or CS1 nanocomposite cylindrical shells are used (see Fig. 3). The laminated cylindrical shells consist of nanocomposite plies with U, V, ◊ and X models.

The sensitivity of functionally graded-nanocomposite cylindrical shells to CNT patterns, SDT formulation, and temperature change is interpreted using the following ratios:

$$100\% \times \left(\frac{N_{1\mathrm{ax}}^{\mathrm{crFG}}-N_{1\mathrm{ax}}^{\mathrm{crU}}}{N_{1\mathrm{ax}}^{\mathrm{crU}}},\ \frac{N_{1\mathrm{ax}}^{\mathrm{crkl}}-N_{1\mathrm{ax}}^{\mathrm{crst}}}{N_{1\mathrm{ax}}^{\mathrm{crst}}},\ \frac{N_{1\mathrm{ax}}^{\mathrm{crT}}-N_{1\mathrm{ax}}^{\mathrm{crT_0}}}{N_{1\mathrm{ax}}^{\mathrm{crT_0}}}\right) \text{ and } 100\% \times \left(\frac{\Omega_1^{\mathrm{FG}}-\Omega_1^{U}}{\Omega_1^{U}},\ \frac{\Omega_1^{kl}-\Omega_1^{\mathrm{st}}}{\Omega_1^{kl}},\ \frac{\Omega_{1\mathrm{T}}-\Omega_{1\mathrm{T_0}}}{\Omega_{1\mathrm{T_0}}}\right).$$

Since in all calculations the longitudinal wave number is equal to one, it is not included in the tables.

Table 5 Distribution of N_{1ax}^{cr} and (n_{cr}) for laminated cylindrical shells consisting of nanocomposite layers against R/h at room temperature ($T = 300$ K) within different theories

		$N_{1ax}^{cr} \times 10$, (n_{cr})							
		U		V		◊		X	
R/h	Number and alignment of plies	SDT	KLT	SDT	KLT	SDT	KLT	SDT	KLT
20	CS1	3.209 (4)	7.777 (4)	2.841 (4)	5.373 (3)	2.540 (4)	4.120 (4)	3.441 (4)	11.47 (3)
	LCS2	1.564 (4)	1.846 (4)	1.766 (4)	2.137 (4)	1.270 (4)	1.407 (4)	1.460 (4)	1.700 (4)
	LCS3a	3.346 (4)	7.677 (4)	2.696 (4)	4.465 (4)	2.590 (4)	3.920 (4)	3.561 (5)	11.46 (4)
	LCS3b	1.353 (3)	1.498 (3)	1.340 (3)	1.438 (3)	1.343 (3)	1.424 (3)	1.413 (3)	1.659 (3)
	LCS4a	2.646 (3)	3.977 (3)	2.687 (4)	4.076 (4)	2.160 (4)	2.750 (4)	2.527 (3)	3.925 (3)
	LCS4b	3.361 (4)	7.150 (4)	2.501 (4)	3.681 (4)	2.401 (4)	3.313 (4)	3.653 (4)	11.03 (4)
	LCS4c	1.776 (3)	2.094 (3)	1.740 (3)	1.990 (3)	1.814 (3)	2.089 (3)	1.784 (3)	2.174 (3)
30	CS1	2.196 (5)	3.571 (5)	1.817 (5)	2.522 (4)	1.533 (5)	1.944 (5)	2.570 (5)	5.228 (4)
	LCS2	0.947 (4)	1.012 (4)	1.020 (5)	1.112 (5)	0.772 (5)	0.809 (5)	0.901 (5)	0.957 (4)
	LCS3a	2.265 (5)	3.559 (5)	1.677 (5)	2.154 (5)	1.559 (5)	1.901 (5)	2.638 (5)	5.245 (5)
	LCS3b	0.973 (3)	1.005 (3)	0.899 (4)	0.953 (4)	0.867 (4)	0.905 (4)	1.038 (3)	1.096 (3)
	LCS4a	1.661 (4)	2.025 (4)	1.677 (4)	2.030 (4)	1.289 (4)	1.425 (4)	1.613 (4)	2.003 (4)
	LCS4b	2.276 (4)	3.370 (4)	1.560 (5)	1.862 (4)	1.457 (4)	1.676 (4)	2.698 (5)	5.101 (4)
	LCS4c	1.195 (3)	1.266 (3)	1.085 (4)	1.164 (4)	1.091 (4)	1.167 (4)	1.234 (3)	1.325 (3)
40	CS1	1.545 (6)	2.079 (5)	1.238 (5)	1.497 (5)	1.015 (6)	1.163 (6)	1.919 (6)	3.016 (5)
	LCS2	0.657 (5)	0.683 (5)	0.694 (5)	0.725 (5)	0.546 (5)	0.558 (5)	0.623 (5)	0.646 (5)
	LCS3a	1.598 (6)	2.099 (5)	1.146 (6)	1.322 (5)	1.053 (5)	1.172 (5)	1.964 (6)	3.047 (6)
	LCS3b	0.744 (4)	0.784 (4)	0.687 (4)	0.705 (4)	0.656 (4)	0.668 (4)	0.853 (4)	0.899 (3)
	LCS4a	1.162 (4)	1.290 (4)	1.148 (5)	1.281 (5)	0.908 (5)	0.961 (4)	1.146 (4)	1.286 (4)
	LCS4b	1.585 (5)	2.005 (5)	1.060 (5)	1.172 (5)	0.982 (5)	1.063 (5)	1.994 (5)	2.975 (5)
	LCS4c	0.866 (4)	0.915 (4)	0.801 (4)	0.828 (4)	0.787 (4)	0.812 (4)	0.965 (4)	1.027 (3)
50	CS1	1.132 (6)	1.376 (6)	0.894 (6)	1.012 (6)	0.727 (6)	0.791 (6)	1.456 (6)	1.983 (6)
	LCS2	0.506 (5)	0.517 (5)	0.516 (6)	0.531 (6)	0.430 (6)	0.437 (6)	0.488 (5)	0.498 (5)
	LCS3a	1.172 (6)	1.400 (6)	0.833 (6)	0.911 (6)	0.760 (6)	0.814 (6)	1.492 (6)	2.007 (6)
	LCS3b	0.610 (4)	0.627 (4)	0.581 (4)	0.589 (4)	0.553 (5)	0.558 (4)	0.695 (4)	0.733 (4)
	LCS4a	0.892 (5)	0.950 (4)	0.853 (5)	0.911 (5)	0.678 (5)	0.701 (5)	0.881 (5)	0.952 (5)
	LCS4b	1.175 (5)	1.364 (5)	0.794 (5)	0.843 (5)	0.731 (5)	0.765 (5)	1.524 (5)	1.988 (5)
	LCS4c	0.690 (4)	0.710 (4)	0.643 (5)	0.663 (5)	0.617 (5)	0.633 (5)	0.768 (4)	0.808 (4)

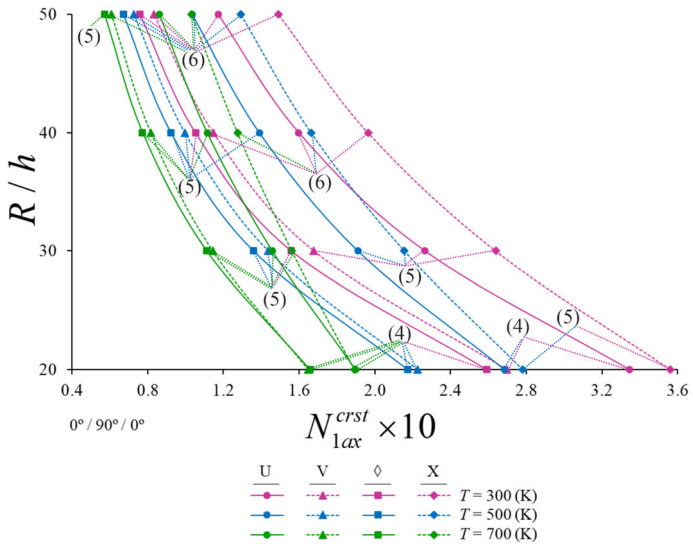

Fig. 4 Variation of N_{1ax}^{crst} and (n_{cr}) for LCS3a array shells with U, X, V and ◊ models in thermal environments against the R/h

Table 6 Distribution of N_{1ax}^{cr} and (n_{cr}) for laminated cylindrical shells consisting of nanocomposite piles against R/h at $T = 500$ K within two different theories

		$N_{1ax}^{cr} \times 10$, (n_{cr})							
		U		V		◊		X	
R/h	Number and alignment of plies	SDT	KLT	SDT	KLT	SDT	KLT	SDT	KLT
20	CS1	3.186 (4)	7.626 (4)	2.816 (4)	5.273 (3)	2.514 (4)	4.045 (4)	3.423 (4)	11.24 (3)
	LCS2	1.549 (4)	1.824 (4)	1.748 (4)	2.109 (4)	1.258 (4)	1.392 (4)	1.450 (4)	1.685 (4)
	LCS3a	3.321 (4)	7.531 (4)	2.672 (4)	4.388 (4)	2.564 (4)	3.851 (4)	3.542 (5)	11.24 (4)
	LCS3b	1.344 (3)	1.484 (3)	1.332 (3)	1.428 (3)	1.333 (3)	1.412 (3)	1.405 (3)	1.645 (3)
	LCS4a	2.621 (3)	3.911 (3)	2.660 (4)	4.008 (4)	2.135 (4)	2.706 (4)	2.506 (3)	3.864 (3)
	LCS4b	3.334 (4)	7.015 (4)	2.477 (4)	3.622 (4)	2.375 (4)	3.257 (4)	3.632 (4)	10.81 (4)
	LCS4c	1.760 (3)	2.068 (3)	1.726 (3)	1.969 (3)	1.796 (3)	2.062 (3)	1.770 (3)	2.149 (3)
30	CS1	2.173 (5)	3.504 (5)	1.795 (5)	2.478 (4)	1.513 (5)	1.910 (5)	2.548 (5)	5.128 (4)
	LCS2	0.939 (4)	1.002 (4)	1.010 (5)	1.098 (5)	0.765 (5)	0.801 (5)	0.894 (5)	0.950 (4)
	LCS3a	2.241 (5)	3.493 (5)	1.657 (5)	2.120 (5)	1.539 (5)	1.870 (5)	2.615 (5)	5.146 (5)
	LCS3b	0.968 (3)	0.998 (3)	0.892 (4)	0.945 (4)	0.859 (4)	0.896 (4)	1.032 (3)	1.089 (3)
	LCS4a	1.641 (4)	1.993 (4)	1.658 (4)	2.000 (4)	1.274 (4)	1.405 (4)	1.595 (4)	1.974 (4)
	LCS4b	2.250 (5)	3.310 (4)	1.542 (5)	1.836 (4)	1.439 (4)	1.651 (4)	2.673 (5)	5.006 (4)
	LCS4c	1.185 (3)	1.254 (3)	1.075 (4)	1.152 (4)	1.079 (4)	1.152 (4)	1.225 (3)	1.313 (3)
40	CS1	1.526 (6)	2.042 (5)	1.222 (5)	1.472 (5)	1.001 (6)	1.144 (6)	1.898 (6)	2.960 (5)
	LCS2	0.651 (5)	0.676 (5)	0.688 (5)	0.718 (5)	0.541 (5)	0.553 (5)	0.619 (5)	0.641 (5)
	LCS3a	1.578 (6)	2.062 (5)	1.132 (6)	1.303 (5)	1.039 (5)	1.155 (5)	1.943 (6)	2.991 (6)
	LCS3b	0.738 (4)	0.776 (4)	0.682 (4)	0.701 (4)	0.651 (4)	0.663 (4)	0.846 (4)	0.895 (3)
	LCS4a	1.148 (4)	1.272 (4)	1.134 (5)	1.263 (5)	0.897 (5)	0.949 (5)	1.134 (4)	1.269 (4)
	LCS4b	1.564 (5)	1.970 (5)	1.048 (5)	1.156 (5)	0.970 (5)	1.048 (5)	1.971 (5)	2.921 (5)
	LCS4c	0.858 (4)	0.904 (4)	0.795 (4)	0.821 (4)	0.779 (4)	0.803 (4)	0.955 (4)	1.020 (3)
50	CS1	1.117 (6)	1.352 (6)	0.882 (6)	0.996 (6)	0.717 (6)	0.779 (6)	1.438 (6)	1.947 (6)
	LCS2	0.502 (5)	0.513 (5)	0.511 (6)	0.526 (6)	0.427 (6)	0.433 (6)	0.485 (5)	0.495 (5)
	LCS3a	1.156 (6)	1.376 (6)	0.823 (6)	0.899 (6)	0.750 (6)	0.802 (6)	1.474 (6)	1.971 (6)
	LCS3b	0.606 (4)	0.622 (4)	0.578 (4)	0.586 (4)	0.547 (5)	0.555 (4)	0.690 (4)	0.727 (4)
	LCS4a	0.880 (5)	0.939 (4)	0.843 (5)	0.899 (5)	0.670 (5)	0.692 (5)	0.870 (5)	0.939 (5)
	LCS4b	1.159 (5)	1.341 (5)	0.786 (5)	0.833 (5)	0.722 (5)	0.755 (5)	1.505 (5)	1.953 (5)
	LCS4c	0.684 (4)	0.703 (4)	0.637 (5)	0.657 (5)	0.610 (5)	0.626 (5)	0.762 (4)	0.800 (4)

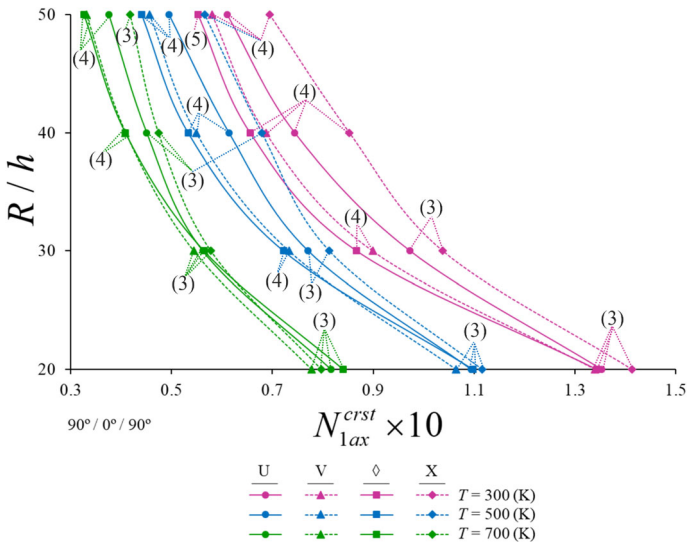

Fig. 5 Variation of N_{1ax}^{crst} and (n_{cr}) for LCS3b array shells with ◊, V, X and U models in thermal environments against the R/h

Table 7 Distribution of N_{1ax}^{cr} and (n_{cr}) for laminated cylindrical shells consisting of nanocomposite piles against R/h at $T = 700$ K within two different theories

		$N_{1ax}^{cr} \times 10$, (n_{cr})							
		U		V		◊		X	
R/h	Number and alignment of plies	SDT	KLT	SDT	KLT	SDT	KLT	SDT	KLT
20	CS1	3.174 (4)	7.553 (4)	2.804 (4)	5.224 (3)	2.501 (4)	4.008 (4)	3.414 (4)	11.13 (3)
	LCS2	1.541 (4)	1.813 (4)	1.739 (4)	2.095 (4)	1.253 (4)	1.385 (4)	1.444 (4)	1.678 (4)
	LCS3a	3.309 (4)	7.460 (4)	2.660 (4)	4.351 (4)	2.551 (4)	3.818 (4)	3.533 (5)	11.13 (4)
	LCS3b	1.339 (3)	1.478 (3)	1.328 (3)	1.423 (3)	1.328 (3)	1.406 (3)	1.401 (3)	1.637 (3)
	LCS4a	2.609 (3)	3.880 (3)	2.647 (4)	3.975 (4)	2.123 (4)	2.685 (4)	2.496 (3)	3.835 (3)
	LCS4b	3.321 (4)	6.949 (4)	2.465 (4)	3.594 (4)	2.362 (4)	3.230 (4)	3.621 (4)	10.71 (4)
	LCS4c	1.751 (3)	2.055 (3)	1.719 (3)	1.958 (3)	1.787 (3)	2.048 (3)	1.763 (3)	2.136 (3)
30	CS1	2.161 (5)	3.471 (5)	1.785 (5)	2.456 (4)	1.504 (5)	1.894 (5)	2.537 (5)	5.079 (4)
	LCS2	0.935 (4)	0.997 (4)	1.004 (5)	1.092 (5)	0.762 (5)	0.797 (5)	0.891 (5)	0.947 (4)
	LCS3a	2.229 (5)	3.461 (5)	1.648 (5)	2.103 (5)	1.530 (5)	1.854 (5)	2.604 (5)	5.097 (5)
	LCS3b	0.965 (3)	0.995 (3)	0.889 (4)	0.941 (4)	0.856 (4)	0.891 (4)	1.030 (3)	1.086 (3)
	LCS4a	1.632 (4)	1.978 (4)	1.649 (4)	1.985 (4)	1.267 (4)	1.396 (4)	1.587 (4)	1.959 (4)
	LCS4b	2.237 (5)	3.281 (4)	1.534 (5)	1.823 (4)	1.431 (4)	1.639 (4)	2.660 (5)	4.959 (4)
	LCS4c	1.180 (3)	1.248 (3)	1.071 (4)	1.146 (4)	1.073 (4)	1.145 (4)	1.221 (3)	1.307 (3)
40	CS1	1.516 (6)	2.024 (5)	1.214 (5)	1.460 (5)	0.994 (6)	1.135 (6)	1.888 (6)	2.932 (5)
	LCS2	0.648 (5)	0.673 (5)	0.684 (5)	0.714 (5)	0.539 (5)	0.551 (5)	0.617 (5)	0.639 (5)
	LCS3a	1.568 (6)	2.044 (5)	1.125 (6)	1.293 (5)	1.033 (5)	1.146 (5)	1.932 (6)	2.963 (6)
	LCS3b	0.735 (4)	0.772 (4)	0.680 (4)	0.698 (4)	0.649 (4)	0.660 (4)	0.843 (4)	0.893 (3)
	LCS4a	1.142 (4)	1.263 (4)	1.127 (5)	1.254 (5)	0.891 (5)	0.943 (5)	1.128 (4)	1.261 (4)
	LCS4b	1.554 (5)	1.953 (5)	1.042 (5)	1.148 (5)	0.964 (5)	1.040 (5)	1.960 (5)	2.894 (5)
	LCS4c	0.854 (4)	0.899 (4)	0.792 (4)	0.818 (4)	0.776 (4)	0.799 (4)	0.951 (4)	1.017 (3)
50	CS1	1.109 (6)	1.340 (6)	0.876 (6)	0.988 (6)	0.712 (6)	0.773 (6)	1.429 (6)	1.929 (6)
	LCS2	0.500 (5)	0.511 (5)	0.509 (6)	0.523 (6)	0.425 (6)	0.431 (6)	0.484 (5)	0.493 (5)
	LCS3a	1.149 (6)	1.365 (6)	0.818 (6)	0.892 (6)	0.745 (6)	0.796 (6)	1.464 (6)	1.953 (6)
	LCS3b	0.604 (4)	0.619 (4)	0.577 (4)	0.584 (4)	0.545 (5)	0.553 (4)	0.687 (4)	0.724 (4)
	LCS4a	0.875 (5)	0.933 (4)	0.838 (5)	0.893 (5)	0.666 (5)	0.688 (5)	0.865 (5)	0.933 (5)
	LCS4b	1.151 (5)	1.330 (5)	0.782 (5)	0.828 (5)	0.718 (5)	0.750 (5)	1.496 (5)	1.936 (5)
	LCS4c	0.681 (4)	0.700 (4)	0.634 (5)	0.653 (5)	0.607 (5)	0.622 (5)	0.759 (4)	0.796 (4)

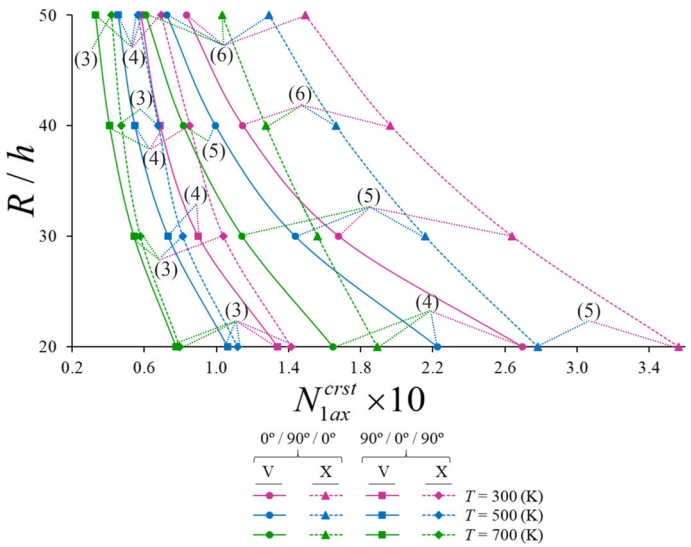

Fig. 6 Variation of N_{1ax}^{crst} and corresponding circumferential wave numbers (n_{cr}) for LCS3a and LCS3b array shells with V and X models in thermal environments against the R/h

Table 8 Distribution of Ω_1 and (n) for laminated cylindrical shells composed of nanocomposite model layers in room temperature ($T = 300$ K) against the R/h

		$\Omega_1/10$ (n)							
		U		V		◊		X	
R/h	Number and alignment of plies	SDT	KLT	SDT	KLT	SDT	KLT	SDT	KLT
20	CS1	1.727 (4)	2.689 (4)	1.626 (4)	2.235 (3)	1.537 (4)	1.957 (4)	1.789 (4)	3.266 (3)
	LCS2	1.206 (4)	1.310 (4)	1.282 (4)	1.410 (4)	1.087 (4)	1.144 (4)	1.165 (4)	1.257 (4)
	LCS3a	1.764 (4)	2.672 (4)	1.583 (4)	2.038 (4)	1.552 (4)	1.909 (4)	1.820 (5)	3.266 (4)
	LCS3b	1.122 (3)	1.180 (3)	1.116 (3)	1.156 (3)	1.118 (3)	1.151 (3)	1.146 (3)	1.242 (3)
	LCS4a	1.569 (3)	1.923 (3)	1.581 (4)	1.947 (4)	1.417 (4)	1.599 (4)	1.533 (3)	1.910 (3)
	LCS4b	1.768 (4)	2.579 (4)	1.525 (4)	1.850 (4)	1.494 (4)	1.755 (4)	1.843 (4)	3.203 (4)
	LCS4c	1.285 (3)	1.395 (3)	1.272 (3)	1.360 (3)	1.299 (3)	1.394 (3)	1.288 (3)	1.422 (3)
30	CS1	2.144 (5)	2.734 (5)	1.950 (5)	2.297 (4)	1.791 (5)	2.017 (5)	2.319 (5)	3.308 (4)
	LCS2	1.408 (4)	1.455 (4)	1.461 (5)	1.525 (5)	1.271 (5)	1.301 (5)	1.373 (5)	1.415 (4)
	LCS3a	2.177 (5)	2.729 (5)	1.873 (5)	2.123 (5)	1.806 (5)	1.995 (5)	2.350 (5)	3.313 (5)
	LCS3b	1.427 (3)	1.450 (3)	1.372 (4)	1.412 (4)	1.347 (4)	1.376 (4)	1.474 (3)	1.514 (3)
	LCS4a	1.864 (4)	2.059 (4)	1.873 (4)	2.061 (4)	1.642 (4)	1.727 (4)	1.837 (4)	2.048 (4)
	LCS4b	2.182 (4)	2.656 (4)	1.807 (5)	1.974 (4)	1.746 (4)	1.873 (4)	2.376 (5)	3.267 (4)
	LCS4c	1.581 (3)	1.628 (3)	1.507 (4)	1.561 (4)	1.511 (4)	1.563 (4)	1.607 (3)	1.665 (3)
40	CS1	2.398 (6)	2.782 (5)	2.146 (5)	2.360 (5)	1.943 (6)	2.080 (6)	2.672 (6)	3.350 (5)
	LCS2	1.564 (5)	1.594 (5)	1.607 (5)	1.643 (5)	1.425 (5)	1.441 (5)	1.523 (5)	1.550 (5)
	LCS3a	2.439 (6)	2.795 (5)	2.065 (6)	2.218 (5)	1.979 (5)	2.089 (5)	2.704 (6)	3.367 (6)
	LCS3b	1.664 (4)	1.708 (4)	1.599 (4)	1.620 (4)	1.562 (4)	1.577 (4)	1.782 (4)	1.829 (3)
	LCS4a	2.079 (4)	2.191 (4)	2.067 (5)	2.184 (5)	1.838 (5)	1.891 (4)	2.065 (4)	2.188 (4)
	LCS4b	2.428 (5)	2.732 (5)	1.986 (5)	2.088 (5)	1.912 (5)	1.989 (5)	2.724 (5)	3.327 (5)
	LCS4c	1.796 (4)	1.845 (4)	1.727 (4)	1.755 (4)	1.711 (4)	1.738 (4)	1.895 (4)	1.955 (3)
50	CS1	2.566 (6)	2.829 (6)	2.280 (6)	2.425 (6)	2.056 (6)	2.145 (6)	2.910 (6)	3.395 (6)
	LCS2	1.716 (5)	1.735 (5)	1.732 (6)	1.757 (6)	1.582 (6)	1.594 (6)	1.685 (5)	1.702 (5)
	LCS3a	2.611 (6)	2.853 (6)	2.201 (6)	2.302 (6)	2.103 (6)	2.175 (6)	2.946 (6)	3.416 (6)
	LCS3b	1.883 (4)	1.909 (4)	1.838 (4)	1.851 (4)	1.793 (5)	1.802 (4)	2.011 (4)	2.065 (4)
	LCS4a	2.278 (5)	2.351 (4)	2.227 (5)	2.302 (5)	1.985 (5)	2.019 (5)	2.263 (5)	2.353 (5)
	LCS4b	2.613 (5)	2.816 (5)	2.149 (5)	2.214 (5)	2.061 (5)	2.109 (5)	2.977 (5)	3.399 (5)
	LCS4c	2.003 (4)	2.032 (4)	1.934 (5)	1.964 (5)	1.894 (5)	1.919 (5)	2.114 (4)	2.168 (4)

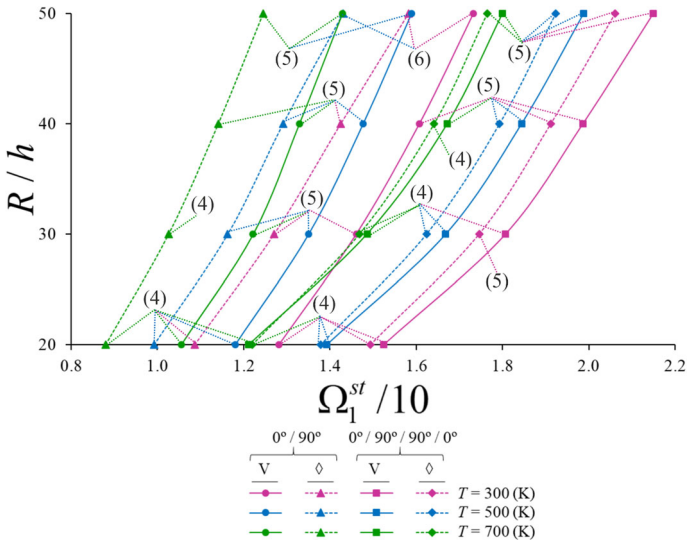

Fig. 7 Variation of Ω_1^{ST} and corresponding wave numbers (n) for LCS2 and LCS4b array shells with U and ◊ models in thermal environments against the R/h

Table 9 Distribution of Ω_1 and (n) for LCSs consisting of nanocomposite plies in thermal environmental against R/h at $T = 500$ K

		$\Omega_1/10, (n)$							
		U		V		◊		X	
R/h	Number and arrangement of plies	SDT	KLT	SDT	KLT	SDT	KLT	SDT	KLT
20	CS1	1.721 (4)	2.663 (4)	1.618 (4)	2.214 (3)	1.529 (4)	1.939 (4)	1.784 (4)	3.234 (3)
	LCS2	1.200 (4)	1.302 (4)	1.275 (4)	1.400 (4)	1.082 (4)	1.138 (4)	1.161 (4)	1.252 (4)
	LCS3a	1.757 (4)	2.646 (4)	1.576 (4)	2.020 (4)	1.544 (4)	1.893 (4)	1.815 (5)	3.234 (4)
	LCS3b	1.118 (3)	1.175 (3)	1.113 (3)	1.152 (3)	1.113 (3)	1.146 (3)	1.143 (3)	1.237 (3)
	LCS4a	1.561 (3)	1.907 (3)	1.573 (4)	1.931 (4)	1.409 (4)	1.586 (4)	1.527 (3)	1.896 (3)
	LCS4b	1.761 (4)	2.554 (4)	1.518 (4)	1.835 (4)	1.486 (4)	1.740 (4)	1.838 (4)	3.172 (4)
	LCS4c	1.279 (3)	1.387 (3)	1.267 (3)	1.353 (3)	1.292 (3)	1.385 (3)	1.283 (3)	1.414 (3)
30	CS1	2.132 (5)	2.708 (5)	1.938 (5)	2.277 (4)	1.780 (5)	1.999 (5)	2.309 (5)	3.276 (4)
	LCS2	1.402 (4)	1.448 (4)	1.454 (5)	1.516 (5)	1.266 (5)	1.294 (5)	1.368 (5)	1.410 (4)
	LCS3a	2.166 (5)	2.704 (5)	1.862 (5)	2.106 (5)	1.795 (5)	1.978 (5)	2.339 (5)	3.282 (5)
	LCS3b	1.423 (3)	1.446 (3)	1.367 (4)	1.406 (4)	1.341 (4)	1.369 (4)	1.470 (3)	1.510 (3)
	LCS4a	1.853 (4)	2.042 (4)	1.863 (4)	2.046 (4)	1.633 (4)	1.715 (4)	1.827 (4)	2.032 (4)
	LCS4b	2.170 (5)	2.632 (4)	1.797 (5)	1.960 (4)	1.736 (4)	1.859 (4)	2.365 (5)	3.237 (4)
	LCS4c	1.575 (3)	1.620 (3)	1.500 (4)	1.553 (4)	1.503 (4)	1.553 (4)	1.601 (3)	1.658 (3)
40	CS1	2.383 (6)	2.756 (5)	2.132 (5)	2.341 (5)	1.930 (6)	2.063 (6)	2.658 (6)	3.319 (5)
	LCS2	1.557 (5)	1.586 (5)	1.600 (5)	1.634 (5)	1.420 (5)	1.435 (5)	1.518 (5)	1.545 (5)
	LCS3a	2.423 (6)	2.770 (5)	2.052 (6)	2.202 (5)	1.967 (5)	2.073 (5)	2.689 (6)	3.336 (6)
	LCS3b	1.657 (4)	1.699 (4)	1.594 (4)	1.615 (4)	1.557 (4)	1.571 (4)	1.775 (4)	1.825 (3)
	LCS4a	2.067 (4)	2.176 (4)	2.054 (5)	2.168 (5)	1.827 (5)	1.880 (5)	2.054 (4)	2.173 (4)
	LCS4b	2.413 (5)	2.708 (5)	1.975 (5)	2.074 (5)	1.900 (5)	1.974 (5)	2.708 (5)	3.297 (5)
	LCS4c	1.787 (4)	1.834 (4)	1.720 (4)	1.748 (4)	1.703 (4)	1.729 (4)	1.885 (4)	1.949 (3)
50	CS1	2.548 (6)	2.804 (6)	2.265 (6)	2.406 (6)	2.042 (6)	2.128 (6)	2.891 (6)	3.364 (6)
	LCS2	1.709 (5)	1.727 (5)	1.724 (6)	1.749 (6)	1.575 (6)	1.587 (6)	1.680 (5)	1.696 (5)
	LCS3a	2.593 (6)	2.829 (6)	2.188 (6)	2.286 (6)	2.089 (6)	2.159 (6)	2.927 (6)	3.385 (6)
	LCS3b	1.877 (4)	1.902 (4)	1.834 (4)	1.846 (4)	1.784 (5)	1.797 (4)	2.003 (4)	2.056 (4)
	LCS4a	2.263 (5)	2.336 (4)	2.214 (5)	2.287 (5)	1.974 (5)	2.007 (5)	2.250 (5)	2.337 (5)
	LCS4b	2.596 (5)	2.793 (5)	2.138 (5)	2.201 (5)	2.049 (5)	2.095 (5)	2.958 (5)	3.369 (5)
	LCS4c	1.994 (4)	2.023 (4)	1.925 (5)	1.954 (5)	1.884 (5)	1.908 (5)	2.105 (4)	2.157 (4)

Table 10 Distribution of Ω_1 and (n) for LCSs built of nanocomposite plies in thermal environmental against R/h at $T = 700$ K

		$\Omega_1/10$ (n)							
		U		V		◊		X	
R/h	Number and arrangement of plies	SDT	KLT	SDT	KLT	SDT	KLT	SDT	KLT
20	CS1	1.718 (4)	2.650 (4)	1.615 (4)	2.204 (3)	1.525 (4)	1.931 (4)	1.782 (4)	3.218 (3)
	LCS2	1.197 (4)	1.298 (4)	1.272 (4)	1.396 (4)	1.079 (4)	1.135 (4)	1.159 (4)	1.249 (4)
	LCS3a	1.754 (4)	2.634 (4)	1.573 (4)	2.012 (4)	1.540 (4)	1.884 (4)	1.813 (5)	3.218 (4)
	LCS3b	1.116 (3)	1.172 (3)	1.111 (3)	1.150 (3)	1.111 (3)	1.143 (3)	1.142 (3)	1.234 (3)
	LCS4a	1.558 (3)	1.899 (3)	1.569 (4)	1.923 (4)	1.405 (4)	1.580 (4)	1.524 (3)	1.888 (3)
	LCS4b	1.757 (4)	2.542 (4)	1.514 (4)	1.828 (4)	1.482 (4)	1.733 (4)	1.835 (4)	3.157 (4)
	LCS4c	1.276 (3)	1.382 (3)	1.264 (3)	1.349 (3)	1.289 (3)	1.380 (3)	1.280 (3)	1.409 (3)
30	CS1	2.127 (5)	2.695 (5)	1.933 (5)	2.267 (4)	1.774 (5)	1.991 (5)	2.304 (5)	3.260 (4)
	LCS2	1.399 (4)	1.445 (4)	1.450 (5)	1.512 (5)	1.263 (5)	1.291 (5)	1.365 (5)	1.408 (4)
	LCS3a	2.160 (5)	2.691 (5)	1.857 (5)	2.098 (5)	1.789 (5)	1.970 (5)	2.334 (5)	3.266 (5)
	LCS3b	1.421 (3)	1.443 (3)	1.364 (4)	1.403 (4)	1.338 (4)	1.366 (4)	1.468 (3)	1.507 (3)
	LCS4a	1.848 (4)	2.034 (4)	1.857 (4)	2.038 (4)	1.628 (4)	1.709 (4)	1.822 (4)	2.025 (4)
	LCS4b	2.164 (5)	2.620 (4)	1.792 (5)	1.953 (4)	1.731 (4)	1.852 (4)	2.360 (5)	3.222 (4)
	LCS4c	1.572 (3)	1.616 (3)	1.497 (4)	1.549 (4)	1.499 (4)	1.548 (4)	1.598 (3)	1.654 (3)
40	CS1	2.375 (6)	2.744 (5)	2.125 (5)	2.331 (5)	1.924 (6)	2.055 (6)	2.650 (6)	3.303 (5)
	LCS2	1.553 (5)	1.582 (5)	1.596 (5)	1.630 (5)	1.417 (5)	1.432 (5)	1.516 (5)	1.542 (5)
	LCS3a	2.415 (6)	2.758 (5)	2.046 (6)	2.194 (5)	1.960 (5)	2.065 (5)	2.681 (6)	3.320 (6)
	LCS3b	1.654 (4)	1.695 (4)	1.591 (4)	1.612 (4)	1.554 (4)	1.568 (4)	1.771 (4)	1.823 (3)
	LCS4a	2.061 (4)	2.168 (4)	2.048 (5)	2.160 (5)	1.821 (5)	1.873 (5)	2.048 (4)	2.166 (4)
	LCS4b	2.405 (5)	2.696 (5)	1.969 (5)	2.067 (5)	1.894 (5)	1.967 (5)	2.701 (5)	3.282 (5)
	LCS4c	1.782 (4)	1.829 (4)	1.717 (4)	1.744 (4)	1.699 (4)	1.725 (4)	1.881 (4)	1.945 (3)
50	CS1	2.540 (6)	2.792 (6)	2.258 (6)	2.397 (6)	2.036 (6)	2.120 (6)	2.882 (6)	3.349 (6)
	LCS2	1.706 (5)	1.724 (5)	1.720 (6)	1.744 (6)	1.572 (6)	1.584 (6)	1.678 (5)	1.694 (5)
	LCS3a	2.584 (6)	2.817 (6)	2.181 (6)	2.278 (6)	2.082 (6)	2.151 (6)	2.918 (6)	3.370 (6)
	LCS3b	1.874 (4)	1.898 (4)	1.831 (4)	1.844 (4)	1.780 (5)	1.794 (4)	1.999 (4)	2.051 (4)
	LCS4a	2.256 (5)	2.329 (4)	2.208 (5)	2.279 (5)	1.969 (5)	2.001 (5)	2.243 (5)	2.329 (5)
	LCS4b	2.587 (5)	2.781 (5)	2.132 (5)	2.194 (5)	2.043 (5)	2.089 (5)	2.949 (5)	3.355 (5)
	LCS4c	1.990 (4)	2.018 (4)	1.921 (5)	1.950 (5)	1.879 (5)	1.902 (5)	2.100 (4)	2.152 (4)

Table 11 Variation of N_{1ax}^{crst} and n_{cr} for LCSs consisting of various nanocomposite model plies against the $V_{cn}^{*(k)}$ for $T = 300$ and 500 K

$V_{cn}^{*(k)}$	Number and alignment of plies	$N_{1ax}^{cr} \times 10$, (n_{cr})							
		U		V		◊		X	
		SDT	KLT	SDT	KLT	SDT	KLT	SDT	KLT
		$T = 300$ K							
0.12	CS1	0.871 (4)	1.074 (4)	0.747 (4)	0.859 (4)	0.623 (4)	0.689 (4)	1.068 (4)	1.463 (4)
	LCS2	0.588 (3)	0.602 (3)	0.586 (4)	0.609 (3)	0.523 (3)	0.531 (3)	0.556 (3)	0.569 (3)
	LCS3a	0.948 (4)	1.141 (4)	0.784 (4)	0.869 (4)	0.718 (4)	0.779 (4)	1.117 (4)	1.505 (4)
	LCS3b	0.908 (2)	0.923 (2)	0.773 (3)	0.826 (3)	0.694 (3)	0.729 (3)	0.947 (2)	0.976 (2)
	LCS4a	0.903 (3)	0.978 (3)	0.849 (3)	0.912 (3)	0.722 (3)	0.754 (3)	0.884 (3)	0.958 (3)
	LCS4b	0.994 (3)	1.151 (3)	0.811 (3)	0.866 (3)	0.726 (3)	0.764 (3)	1.192 (3)	1.537 (3)
	LCS4c	0.945 (3)	0.974 (2)	0.788 (3)	0.830 (3)	0.708 (3)	0.739 (3)	0.998 (2)	1.029 (2)
0.17	CS1	1.363 (4)	1.630 (4)	1.174 (4)	1.319 (4)	0.979 (4)	1.062 (4)	1.678 (4)	2.214 (4)
	LCS2	0.951 (3)	0.972 (3)	0.934 (4)	0.970 (4)	0.855 (3)	0.866 (3)	0.919 (3)	0.938 (3)
	LCS3a	1.476 (4)	1.732 (4)	1.225 (4)	1.336 (4)	1.119 (4)	1.196 (4)	1.750 (4)	2.277 (4)
	LCS3b	1.444 (3)	1.515 (2)	1.225 (3)	1.292 (3)	1.103 (3)	1.147 (3)	1.566 (2)	1.605 (2)
	LCS4a	1.414 (3)	1.513 (3)	1.340 (3)	1.423 (3)	1.143 (3)	1.183 (3)	1.395 (3)	1.497 (3)
	LCS4b	1.557 (3)	1.763 (3)	1.282 (3)	1.353 (3)	1.148 (3)	1.196 (3)	1.871 (3)	2.337 (3)
	LCS4c	1.480 (3)	1.587 (2)	1.249 (3)	1.303 (3)	1.121 (3)	1.160 (3)	1.643 (2)	1.683 (2)
0.28	CS1	1.846 (4)	2.398 (4)	1.580 (4)	1.866 (4)	1.317 (4)	1.474 (4)	2.253 (4)	3.386 (4)
	LCS2	1.193 (3)	1.229 (3)	1.185 (3)	1.223 (3)	1.066 (3)	1.083 (3)	1.166 (3)	1.198 (3)
	LCS3a	2.023 (4)	2.550 (4)	1.618 (4)	1.825 (4)	1.538 (4)	1.672 (3)	2.364 (4)	3.479 (4)
	LCS3b	1.790 (2)	1.829 (2)	1.579 (3)	1.708 (3)	1.469 (3)	1.554 (3)	1.949 (2)	2.036 (2)
	LCS4a	1.923 (3)	2.128 (3)	1.755 (3)	1.910 (3)	1.538 (3)	1.613 (3)	1.905 (3)	2.127 (3)
	LCS4b	2.108 (3)	2.542 (3)	1.650 (3)	1.781 (3)	1.546 (3)	1.637 (3)	2.519 (3)	3.517 (3)
	LCS4c	1.907 (2)	1.955 (2)	1.603 (3)	1.702 (3)	1.506 (3)	1.579 (3)	2.067 (2)	2.159 (2)
		$T = 500$ K							
0.12	CS1	0.736 (4)	0.974 (4)	0.624 (4)	0.754 (4)	0.520 (4)	0.598 (4)	0.895 (4)	1.353 (4)
	LCS2	0.469 (3)	0.484 (3)	0.468 (3)	0.487 (3)	0.409 (3)	0.418 (3)	0.434 (3)	0.445 (3)
	LCS3a	0.808 (4)	1.035 (4)	0.654 (4)	0.748 (4)	0.602 (3)	0.663 (3)	0.940 (4)	1.391 (4)
	LCS3b	0.697 (2)	0.714 (2)	0.631 (3)	0.691 (3)	0.572 (3)	0.614 (3)	0.731 (2)	0.766 (2)
	LCS4a	0.767 (3)	0.856 (3)	0.701 (3)	0.773 (3)	0.601 (3)	0.639 (3)	0.745 (3)	0.831 (3)
	LCS4b	0.840 (3)	1.028 (3)	0.661 (3)	0.722 (3)	0.604 (3)	0.649 (3)	1.001 (3)	1.406 (3)
	LCS4c	0.745 (2)	0.766 (2)	0.642 (3)	0.688 (3)	0.588 (3)	0.625 (3)	0.779 (2)	0.816 (2)
0.17	CS1	1.152 (4)	1.469 (4)	0.980 (4)	1.149 (4)	0.816 (4)	0.914 (4)	1.409 (4)	2.035 (4)
	LCS2	0.755 (3)	0.776 (3)	0.753 (3)	0.778 (3)	0.665 (3)	0.677 (3)	0.712 (3)	0.730 (3)
	LCS3a	1.259 (4)	1.561 (4)	1.019 (4)	1.143 (4)	0.949 (4)	1.029 (3)	1.476 (4)	2.092 (4)
	LCS3b	1.144 (2)	1.167 (2)	0.996 (3)	1.073 (3)	0.905 (3)	0.958 (3)	1.205 (2)	1.252 (2)
	LCS4a	1.197 (3)	1.314 (3)	1.103 (3)	1.198 (3)	0.946 (3)	0.994 (3)	1.170 (3)	1.287 (3)

Table 11 continued

$V_{cn}^{*(k)}$	Number and alignment of plies	$N_{1ax}^{cr} \times 10$, (n_{cr})							
		U		V		◊		X	
		SDT $T = 300$ K	KLT	SDT	KLT	SDT	KLT	SDT	KLT
	LCS4b	1.315 (3)	1.562 (3)	1.042 (3)	1.121 (3)	0.951 (3)	1.008 (3)	1.573 (3)	2.124 (3)
	LCS4c	1.214 (2)	1.242 (2)	1.013 (3)	1.073 (3)	0.927 (3)	0.973 (3)	1.277 (2)	1.326 (2)
0.28	CS1	1.558 (4)	2.207 (4)	1.330 (4)	1.666 (4)	1.116 (4)	1.304 (4)	1.862 (4)	3.157 (4)
	LCS2	0.965 (3)	1.003 (3)	0.952 (3)	0.993 (3)	0.844 (3)	0.862 (3)	0.916 (3)	0.946 (3)
	LCS3a	1.727 (4)	2.330 (3)	1.367 (4)	1.594 (3)	1.295 (3)	1.446 (3)	1.967 (4)	3.241 (4)
	LCS3b	1.381 (2)	1.429 (2)	1.305 (3)	1.404 (2)	1.227 (3)	1.330 (3)	1.507 (2)	1.612 (2)
	LCS4a	1.648 (3)	1.895 (3)	1.468 (3)	1.650 (3)	1.297 (3)	1.388 (3)	1.610 (3)	1.869 (3)
	LCS4b	1.787 (3)	2.304 (3)	1.364 (3)	1.514 (3)	1.303 (3)	1.414 (3)	2.095 (3)	3.248 (3)
	LCS4c	1.498 (2)	1.556 (2)	1.323 (3)	1.437 (3)	1.269 (3)	1.357 (3)	1.619 (2)	1.729 (2)

Table 12 Distribution of N_{1ax}^{crst} and n_{cr} for laminated cylindrical shells composed of various nanocomposite model plies against the $V_{cn}^{*(k)}$ in the $T = 700$ K

		$N_{1ax}^{cr} \times 10$, (n_{cr}), $T = 700$ K							
		U		V		◊		X	
$V_{cn}^{*(k)}$	Number and alignment of plies	SDT	KLT	SDT	KLT	SDT	KLT	SDT	KLT
0.12	CS1	0.574 (4)	0.882 (4)	0.487 (4)	0.653 (4)	0.407 (4)	0.510 (4)	0.684 (4)	1.255 (4)
	LCS2	0.349 (3)	0.367 (3)	0.344 (3)	0.365 (3)	0.295 (3)	0.304 (3)	0.310 (3)	0.322 (3)
	LCS3a	0.637 (3)	0.921 (3)	0.507 (3)	0.616 (3)	0.467 (3)	0.550 (3)	0.725 (4)	1.288 (4)
	LCS3b	0.480 (2)	0.503 (2)	0.466 (2)	0.478 (2)	0.444 (3)	0.454 (2)	0.507 (2)	0.554 (2)
	LCS4a	0.620 (3)	0.709 (2)	0.544 (3)	0.637 (3)	0.474 (3)	0.525 (3)	0.596 (3)	0.691 (2)
	LCS4b	0.663 (3)	0.911 (3)	0.505 (3)	0.580 (3)	0.475 (3)	0.537 (3)	0.772 (3)	1.286 (3)
	LCS4c	0.528 (2)	0.557 (2)	0.490 (3)	0.530 (2)	0.464 (3)	0.511 (2)	0.553 (2)	0.602 (2)
0.17	CS1	0.905 (4)	1.319 (4)	0.766 (4)	0.986 (4)	0.640 (4)	0.772 (4)	1.083 (4)	1.873 (4)
	LCS2	0.556 (3)	0.580 (3)	0.547 (3)	0.576 (3)	0.474 (3)	0.487 (3)	0.504 (3)	0.521 (3)
	LCS3a	1.006 (3)	1.387 (3)	0.797 (3)	0.941 (3)	0.737 (3)	0.842 (3)	1.144 (4)	1.922 (4)
	LCS3b	0.784 (2)	0.815 (2)	0.756 (3)	0.785 (2)	0.699 (3)	0.745 (2)	0.832 (2)	0.896 (2)
	LCS4a	0.964 (3)	1.115 (2)	0.853 (3)	0.974 (3)	0.743 (3)	0.807 (3)	0.929 (3)	1.083 (3)
	LCS4b	1.040 (3)	1.371 (3)	0.792 (3)	0.890 (3)	0.745 (3)	0.823 (3)	1.219 (3)	1.926 (3)
	LCS4c	0.855 (2)	0.892 (2)	0.768 (3)	0.843 (3)	0.727 (3)	0.789 (3)	0.900 (2)	0.966 (2)
0.28	CS1	1.207 (4)	2.035 (4)	1.042 (4)	1.479 (4)	0.889 (4)	1.143 (4)	1.385 (4)	2.956 (4)
	LCS2	0.733 (3)	0.780 (3)	0.714 (3)	0.764 (3)	0.619 (3)	0.641 (3)	0.664 (3)	0.695 (3)
	LCS3a	1.339 (3)	2.110 (3)	1.062 (3)	1.347 (3)	1.021 (3)	1.228 (3)	1.482 (4)	3.024 (3)
	LCS3b	0.961 (2)	1.028 (2)	0.933 (2)	0.963 (2)	0.918 (2)	0.937 (2)	1.046 (2)	1.187 (2)
	LCS4a	1.306 (2)	1.519 (2)	1.159 (3)	1.396 (3)	1.044 (3)	1.170 (3)	1.283 (3)	1.510 (2)
	LCS4b	1.409 (3)	2.084 (3)	1.059 (3)	1.252 (3)	1.044 (3)	1.197 (3)	1.585 (3)	3.006 (3)
	LCS4c	1.075 (2)	1.156 (2)	1.029 (3)	1.082 (2)	1.020 (3)	1.078 (2)	1.152 (2)	1.301 (2)

Table 13 Variation of Ω_1 and (n) for laminated cylindrical shells consisting of various nanocomposite model plies against the $V_{\mathrm{cn}}^{*(k)}$ in $T = 300$ and 500 K within two theories

		$\Omega_1/10$, (n)							
		U		V		◊		X	
$V_{cn}^{*(k)}$	Number and alignment of plies	SDT	KLT	SDT	KLT	SDT	KLT	SDT	KLT
		$T = 300$ K							
0.12	CS1	1.831 (4)	2.033 (4)	1.696 (4)	1.818 (4)	1.548 (4)	1.629 (4)	2.027 (4)	2.373 (4)
	LCS2	1.504 (3)	1.522 (3)	1.501 (4)	1.531 (3)	1.419 (3)	1.430 (3)	1.463 (3)	1.479 (3)
	LCS3a	1.909 (4)	2.095 (4)	1.737 (4)	1.828 (4)	1.662 (4)	1.731 (4)	2.073 (4)	2.406 (4)
	LCS3b	1.869 (2)	1.884 (2)	1.725 (3)	1.782 (3)	1.634 (3)	1.675 (3)	1.909 (2)	1.938 (2)
	LCS4a	1.864 (3)	1.940 (3)	1.807 (3)	1.874 (3)	1.667 (3)	1.704 (3)	1.844 (3)	1.920 (3)
	LCS4b	1.955 (3)	2.104 (3)	1.766 (3)	1.825 (3)	1.671 (3)	1.715 (3)	2.141 (3)	2.432 (3)
	LCS4c	1.907 (3)	1.936 (2)	1.741 (3)	1.787 (3)	1.651 (3)	1.686 (3)	1.960 (2)	1.989 (2)
0.17	CS1	2.278 (4)	2.491 (4)	2.114 (4)	2.241 (4)	1.931 (4)	2.011 (4)	2.528 (4)	2.903 (4)
	LCS2	1.903 (3)	1.924 (3)	1.886 (4)	1.922 (4)	1.804 (3)	1.816 (3)	1.871 (3)	1.890 (3)
	LCS3a	2.371 (4)	2.567 (4)	2.159 (4)	2.255 (4)	2.064 (4)	2.134 (4)	2.581 (4)	2.944 (4)
	LCS3b	2.344 (3)	2.401 (2)	2.159 (3)	2.218 (3)	2.049 (3)	2.090 (3)	2.442 (2)	2.472 (2)
	LCS4a	2.320 (3)	2.400 (3)	2.258 (3)	2.328 (3)	2.086 (3)	2.122 (3)	2.305 (3)	2.387 (3)
	LCS4b	2.434 (3)	2.590 (3)	2.209 (3)	2.269 (3)	2.091 (3)	2.134 (3)	2.669 (3)	2.983 (3)
	LCS4c	2.373 (3)	2.458 (2)	2.180 (3)	2.228 (3)	2.066 (3)	2.101 (3)	2.501 (2)	2.531 (2)
0.28	CS1	2.621 (4)	2.987 (4)	2.425 (4)	2.635 (4)	2.214 (4)	2.342 (4)	2.895 (4)	3.549 (4)
	LCS2	2.107 (3)	2.138 (3)	2.100 (3)	2.134 (3)	1.992 (3)	2.008 (3)	2.083 (3)	2.112 (3)
	LCS3a	2.743 (4)	3.080 (4)	2.454 (4)	2.606 (4)	2.392 (4)	2.494 (3)	2.966 (4)	3.598 (4)
	LCS3b	2.581 (2)	2.609 (2)	2.424 (3)	2.521 (3)	2.338 (3)	2.404 (3)	2.693 (2)	2.752 (2)
	LCS4a	2.675 (3)	2.814 (3)	2.555 (3)	2.666 (3)	2.392 (3)	2.450 (3)	2.662 (3)	2.813 (3)
	LCS4b	2.801 (3)	3.075 (3)	2.478 (3)	2.574 (3)	2.398 (3)	2.468 (3)	3.062 (3)	3.617 (3)
	LCS4c	2.664 (2)	2.697 (2)	2.442 (3)	2.517 (3)	2.368 (3)	2.424 (3)	2.773 (2)	2.834 (2)
		$T = 500$ K							
0.12	CS1	1.682 (4)	1.936 (4)	1.550 (4)	1.703 (4)	1.415 (4)	1.517 (4)	1.856 (4)	2.282 (4)
	LCS2	1.344 (3)	1.365 (3)	1.343 (3)	1.369 (3)	1.255 (3)	1.268 (3)	1.292 (3)	1.309 (3)
	LCS3a	1.763 (4)	1.996 (4)	1.586 (4)	1.697 (4)	1.522 (3)	1.597 (3)	1.902 (4)	2.313 (4)
	LCS3b	1.637 (2)	1.657 (2)	1.559 (3)	1.630 (3)	1.483 (3)	1.537 (3)	1.677 (2)	1.716 (2)
	LCS4a	1.718 (3)	1.815 (3)	1.642 (3)	1.725 (3)	1.520 (3)	1.568 (3)	1.694 (3)	1.788 (3)
	LCS4b	1.797 (3)	1.988 (3)	1.595 (3)	1.667 (3)	1.524 (3)	1.581 (3)	1.963 (3)	2.326 (3)
	LCS4c	1.693 (2)	1.717 (2)	1.572 (3)	1.627 (3)	1.505 (3)	1.551 (3)	1.732 (2)	1.772 (2)
0.17	CS1	2.095 (4)	2.365 (4)	1.932 (4)	2.091 (4)	1.762 (4)	1.866 (4)	2.316 (4)	2.783 (4)
	LCS2	1.695 (3)	1.719 (3)	1.693 (3)	1.721 (3)	1.592 (3)	1.605 (3)	1.647 (3)	1.667 (3)
	LCS3a	2.189 (4)	2.438 (4)	1.969 (4)	2.086 (4)	1.901 (4)	1.979 (3)	2.370 (4)	2.822 (4)
	LCS3b	2.087 (2)	2.108 (2)	1.947 (3)	2.021 (3)	1.856 (3)	1.910 (3)	2.142 (2)	2.183 (2)
	LCS4a	2.135 (3)	2.237 (3)	2.049 (3)	2.135 (3)	1.898 (3)	1.945 (3)	2.110 (3)	2.214 (3)

Table 13 continued

$V_{cn}^{*(k)}$	Number and alignment of plies	$\Omega_1/10$, (n)							
		U		V		◊		X	
		SDT	KLT	SDT	KLT	SDT	KLT	SDT	KLT
	LCS4b	2.237 (3)	2.439 (3)	1.992 (3)	2.066 (3)	1.903 (3)	1.959 (3)	2.447 (3)	2.844 (3)
	LCS4c	2.150 (2)	2.174 (2)	1.963 (3)	2.021 (3)	1.879 (3)	1.925 (3)	2.205 (2)	2.247 (2)
0.28	CS1	2.408 (4)	2.866 (4)	2.225 (4)	2.490 (4)	2.038 (4)	2.202 (4)	2.632 (4)	3.427 (4)
	LCS2	1.895 (3)	1.932 (3)	1.882 (3)	1.922 (3)	1.772 (3)	1.791 (3)	1.846 (3)	1.877 (3)
	LCS3a	2.535 (4)	2.944 (3)	2.255 (4)	2.436 (3)	2.195 (3)	2.320 (3)	2.705 (4)	3.472 (4)
	LCS3b	2.267 (2)	2.306 (2)	2.203 (3)	2.286 (2)	2.136 (3)	2.225 (3)	2.368 (2)	2.449 (2)
	LCS4a	2.477 (3)	2.655 (3)	2.337 (3)	2.477 (3)	2.197 (3)	2.273 (3)	2.448 (3)	2.637 (3)
	LCS4b	2.579 (3)	2.928 (3)	2.253 (3)	2.373 (3)	2.202 (3)	2.293 (3)	2.792 (3)	3.477 (3)
	LCS4c	2.361 (2)	2.406 (2)	2.219 (3)	2.312 (3)	2.173 (3)	2.247 (3)	2.455 (2)	2.537 (2)

Table 14 Distribution of Ω_1 and (n) for laminated cylindrical shells composed of various nanocomposite model plies against the $V_{cn}^{*(k)}$ in the $T = 700$ K within two theories

		$\Omega_1/10$, (n), $T = 700$ K							
		U		V		◊		X	
$V_{cn}^{*(k)}$	Number and alignment of plies	SDT	KLT	SDT	KLT	SDT	KLT	SDT	KLT
0.12	CS1	1.487 (4)	1.842 (4)	1.369 (4)	1.586 (4)	1.252 (4)	1.401 (4)	1.622 (4)	2.198 (4)
	LCS2	1.159 (3)	1.188 (3)	1.150 (3)	1.185 (3)	1.065 (3)	1.082 (3)	1.093 (3)	1.113 (3)
	LCS3a	1.566 (3)	1.883 (3)	1.396 (3)	1.539 (3)	1.341 (3)	1.454 (3)	1.671 (4)	2.226 (4)
	LCS3b	1.359 (2)	1.392 (2)	1.339 (2)	1.357 (2)	1.307 (3)	1.321 (2)	1.397 (2)	1.461 (2)
	LCS4a	1.544 (3)	1.652 (2)	1.447 (3)	1.565 (3)	1.351 (3)	1.422 (3)	1.514 (3)	1.630 (2)
	LCS4b	1.597 (3)	1.872 (3)	1.393 (3)	1.494 (3)	1.353 (3)	1.437 (3)	1.724 (3)	2.224 (3)
	LCS4c	1.425 (2)	1.463 (2)	1.373 (3)	1.428 (2)	1.336 (3)	1.402 (2)	1.459 (2)	1.522 (2)
0.17	CS1	1.857 (4)	2.241 (4)	1.708 (4)	1.937 (4)	1.562 (4)	1.714 (4)	2.030 (4)	2.670 (4)
	LCS2	1.455 (3)	1.486 (3)	1.444 (3)	1.481 (3)	1.344 (3)	1.362 (3)	1.386 (3)	1.408 (3)
	LCS3a	1.957 (3)	2.298 (3)	1.742 (3)	1.892 (3)	1.675 (3)	1.791 (3)	2.087 (4)	2.705 (4)
	LCS3b	1.728 (2)	1.762 (2)	1.697 (3)	1.729 (2)	1.632 (3)	1.684 (2)	1.779 (2)	1.847 (2)
	LCS4a	1.916 (3)	2.060 (2)	1.802 (3)	1.926 (3)	1.681 (3)	1.753 (3)	1.881 (3)	2.030 (3)
	LCS4b	1.990 (3)	2.285 (3)	1.736 (3)	1.841 (3)	1.685 (3)	1.770 (3)	2.154 (3)	2.708 (3)
	LCS4c	1.804 (2)	1.843 (2)	1.710 (3)	1.792 (3)	1.663 (3)	1.733 (3)	1.851 (2)	1.918 (2)
0.28	CS1	2.120 (4)	2.752 (4)	1.969 (4)	2.346 (4)	1.819 (4)	2.062 (4)	2.271 (4)	3.317 (4)
	LCS2	1.652 (3)	1.703 (3)	1.631 (3)	1.686 (3)	1.518 (3)	1.545 (3)	1.572 (3)	1.608 (3)
	LCS3a	2.232 (3)	2.802 (3)	1.988 (3)	2.239 (3)	1.949 (3)	2.137 (3)	2.349 (4)	3.354 (3)
	LCS3b	1.892 (2)	1.955 (2)	1.864 (2)	1.893 (2)	1.848 (2)	1.868 (2)	1.973 (2)	2.102 (2)
	LCS4a	2.205 (2)	2.378 (2)	2.076 (3)	2.279 (3)	1.971 (3)	2.087 (3)	2.185 (3)	2.371 (2)
	LCS4b	2.290 (3)	2.785 (3)	1.985 (3)	2.158 (3)	1.971 (3)	2.110 (3)	2.429 (3)	3.344 (3)
	LCS4c	2.000 (2)	2.074 (2)	1.957 (3)	2.006 (2)	1.948 (3)	2.003 (2)	2.071 (2)	2.200 (2)

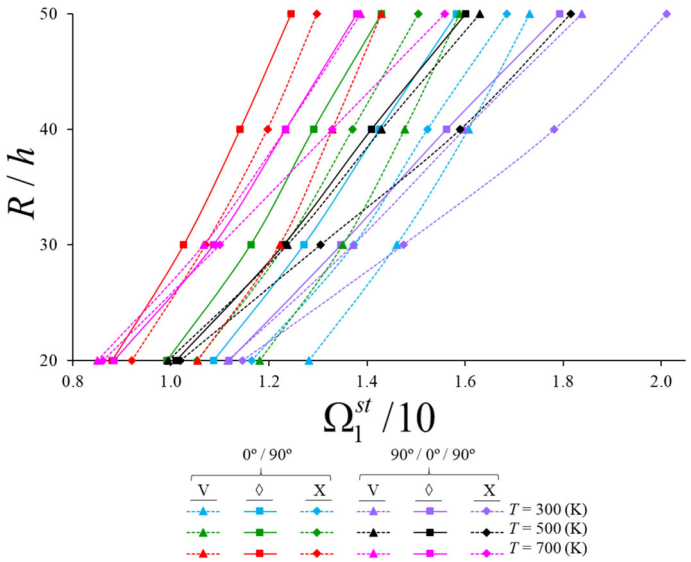

Fig. 8 Variation of Ω_1^{ST} for LCS2 and LCS3b array cylindrical shells with nanocomposite-plies with V, ◊ and X models in thermal environments against the R/h

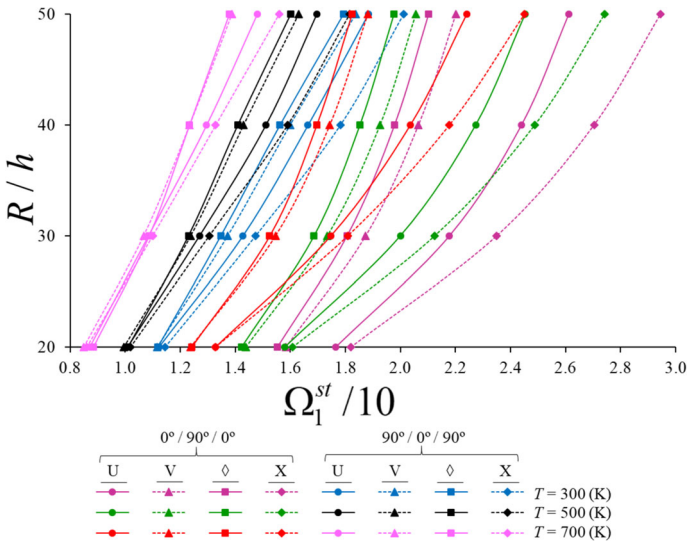

Fig. 9 Variation of Ω_1^{ST} for LCS3a and LCS3b array cylindrical shells with nanocomposite-plies with V, ◊ and X models in thermal environments against the R/h

In Tables 5, 6 and 7 and Figs. 4, 5 and 6, the distribution of the values of the non-dimensional critical axial load (N_{1ax}^{cr}) and corresponding circumferential wave numbers (n_{cr}) for laminated cylindrical shells consisting of three types of FG-nanocomposite plies, such as X, V and ◊ models against the R/h considering the CNT volume fraction $V_{cn}^{*(k)} = 0.28$, thermal environmental conditions $T = 300,\ 500$ and 700 K and $L/R = 0.5$ within SDT and K–L theory are presented. The dimensionless critical axial load values of the U model nanocomposite cylindrical shells are listed in the same table for the comparison purposes. The values of N_{1ax}^{cr} for laminated cylindrical shells with all nanocomposite plies decrease, while corresponding circumferential wave numbers (n_{cr}) increase as the R/h rises.

In the SDT framework, at $T = 300$, 500 and 700 K, the most pronounced V, ◊ and X-model effects on the N_{1ax}^{crst} appear in shells with LCS3b alignments and significant rise with the increase of the R/h ratio. For instance, at $T = 300$ K and $R/h = 20$, the most pronounced V, ◊ and X-models influences on the N_{1ax}^{crst} are (− 25.6%), (− 28.6%) and (+ 8.7%), respectively, as $R/h = 20$, whereas those influences are (− 32.4%), (− 37.8%) and (+ 29.7%), respectively, at $R/h = 50$. In comparison with the $T = 300$ K case, the influences of

the patterns on the N_{1ax}^{crst} at $T = 700$ K reduce by 6.2%, 10.1%, 8%, respectively, for $R/h = 20$, those decrease by 3.1%, 0.3%, 7%, respectively, for $R/h = 50$. Although the influences of shear deformations (SDs) on the critical axial load reduce in all arranged cylindrical shells as the R/h ratio increases, the influences of SDs shows significant differences when the number, arrangement and model of plies change. The most pronounced influences of SDs on the critical axial load appear in the shells with LCS3a alignments. For instance, at $T = 300$ K and $R/h = 20$, the most pronounced influences of SDs on the critical axial load are (+ 56.4%), (+ 39.6%), (+ 33.9%) and (+ 68.9%), respectively, occur in the U, V, ◊ and X models, respectively, whereas as $R/h = 50$, the most evident SDs influences are (+ 16.3%), (+ 8.6%), (+ 6.6%) and (+ 25.7%), respectively. For $T = 500$ K and at $R/h = 20$, the SDs effects on the critical axial load increase by around 7.2%, 7.2%, 7.1% and 6%, respectively, compared to $T = 300$ K, while for $R/h = 50$, those influences rise by around 4.8%, 3%, 2.3% and 5.5%, respectively. At $R/h = 20$, the SDs effects on the critical load for $T = 700$ K increase by around 17%, 18.6%, 18.6% and 13.6%, respectively, compared to $T = 300$ K, while for $R/h = 50$, those influences reduce by around 14%, 8.8%, 7.1% and 17.6%, respectively (see Fig. 4, also).

The most pronounced influence of ply arrangement on the N_{1ax}^{crst} of laminated nanocomposite cylindrical shells occurs at LCS3b arrangement for different temperature and R/h ratio. In addition, as T increases, the arrangement influence reduces for U and X models, while it changes irregularly for V and ◊ models as $R/h = 20$. When T increases, those influences increase significantly for all models as $R/h = 50$. For instance, at $R/h = 20$ for $T = 300$ K, the most pronounced influences of arrangements on the critical axial load are (− 57.84%), (− 52.83%), (− 47.13%) and (− 58.94%), respectively, for $T = 500$ K, those influence are (− 57.38%), (− 54.34%), (− 48.38%) and (− 58.31%), respectively, and for $T = 700$ K those influence are (− 54.72%), (− 54.21%), (− 47.54%) and (− 56.04%), respectively, occur in the U, V, ◊ and X models, respectively (see Fig. 5).

As the $T = 500$ K and $T = 700$ K cases are compared to the $T = 300$ K, the most significant effects of temperature on the N_{1ax}^{crst} occur in the LCS3a and LCS3b arrangements for $R/h = 20$ with different models, while those influences occur in LCS3b arrangement at the radius to thickness ratio is fifty and temperature is 700 K. For instance, at $R/h = 20$, the most pronounced influences of temperature on the critical axial load occur in the U and X models of LCS3a sequence shells, are (− 43.3%) and (− 46.8%), respectively, while those influences are (− 41.9%) and (− 37.4%) occur in the V and ◊ models of LCS3b arrangement shells, respectively. At $R/h = 50$, the most pronounced influences of temperature on the critical axial load for LCS3b arrangement are (− 38.4%), (− 43%), (− 40.9%) and (− 39.9%), respectively, occur in the U, V, ◊ and X models, respectively (see Fig. 6).

In Tables 8, 9 and 10 and Figs. 7, 8 and 9, the distribution of the values of non-dimensional frequency parameter (Ω_1) and corresponding circumferential wave numbers (n) for laminated cylindrical shells with four types of nanocomposite-plies such as U, V, ◊ and X models against the R/h considering $V_{cn}^{*(k)} = 0.28$, $T = 300$, 500 and 700 K and $L/R = 0.5$ within SDT and K–L theory are presented. The values of Ω_1 for laminated cylindrical shells with all nanocomposite plies decrease, whereas corresponding circumferential wave numbers (n) increase as the R/h rises.

Within SDT, as the temperature varies between 300 and 700 K and if the R/h ratio increases, the influences of V, ◊ and X-models on the Ω_1^{st} appear in LCS4b. For instance, at $T = 300$ K, the most prominent influences of the V, ◊ and X models on the Ω_1^{ST} occur in the cylinder with LCS4c arrangement with (− 13.7%), (− 15.5%) and (+ 4.2%), respectively, as $R/h = 20$, while those influences are (− 17.8%), (− 21.1%) and (+ 13.93%), respectively, as $R/h = 50$. At $T = 700$ K, the most prominent influence of the V model on the Ω_1^{st} emerges in the LCS4b with (− 10.3%), those influence are (− 10.6%) and (+ 6.4%) occur in the LCS2 with ◊ and X models, respectively, as $R/h = 20$, while those influences for the V, ◊ and X models are (− 19.7%), (− 21.3%) and (+ 10.8%), respectively, as $R/h = 50$ (see Fig. 7).

Although the influences of shear deformations on the dimensionless frequency parameter diminish with the increase of radius to thickness ratio in all arranged cylindrical shells, while those influences increase with the increasing of the temperature and the most prominent SDs effects on the dimensionless frequency occur in the LCS3a with U, V, ◊ and X patterned layers. For example, at $T = 300$ K and $R/h = 20$, the most evident SDs effects on the dimensionless frequency parameter are (+ 34%), (+ 22.3%), (+ 18.7%) and (+ 44.3%) for U, V, ◊ and X model layers, respectively. While at $R/h = 50$, those effects reduce and are (+ 8.5%), (+ 4.4%), (+ 3.3%) and (+ 13.8%), respectively. In comparison with the $T = 300$ K case, the increase of T rise SDs effects on the dimensionless frequency parameter. For example at $T = 500$ K, the SDs effects on the dimensionless frequency parameter rise by approximately 5.7%, 4.8%, 4.6% and 5.7% as $R/h = 20$ and 2.7%, 1.5%, 1.2% and 3.9%, respectively, for U, V, ◊ and X model layers, as $R/h = 50$. While at $T = 700$ K, those influences

rise by approximately 14.5%, 13.1%, 12.5% and 13.9%, as $R/h = 20$ and 8%, 4.7%, 3.8% and 10.9% for U, V, ◊ and X model layers, respectively, as $R/h = 50$, in comparison with the $T = 300$ K case.

The influence of layer arrangement on the Ω_1^{st} of cylindrical shells changes irregularly with the increase of R/h ratio. For example, at $T = 300$ K, the most significant alignment effects on the Ω_1^{st} of the U and V model shells with LCS3b alignment occur at the $R/h = 20$ with (− 35%) and (− 31.4%), respectively, that influence occurs at $R/h = 20$ in the ◊ patterned shell with LCS2 alignment with (− 29.3%), in the X patterned shell with LCS2 alignment that influence occurs at the $R/h = 40$ with (− 43%), respectively. Compared to $T = 300$ K, at $T = 500$ K the effect of the alignments increases in most cases, and the most significant alignment effects on the Ω_1^{st} of the U and V model shells with LCS3b alignment occur at the $R/h = 20$ with (− 32.7%) and (− 32.4%), respectively, that influence occurs at the $R/h = 20$ in the ◊ patterned shell with LCS2 alignment with (− 31.8%), it occurs at $R/h = 40$ with (− 46.3%) in the FGX patterned shell with LCS3b alignment. At $T = 700$ K, the most significant alignment effects on the Ω_1^{st} of the U model shell with LCS3b alignment occur at the $R/h = 20$ with (− 32.4%), it is (− 35.9%) in the V model shell with LCS2 alignment occur at the $R/h = 40$ with (− 32.4%), that influence occurs at the $R/h = 30$ in the ◊ patterned shell with LCS2 alignment with (− 35.9%) and it occurs at the $R/h = 50$ with (− 44.5%) in the FGX patterned shell with LCS2 alignment (see Fig. 8).

As the $T = 500$ and 700 K cases are compared to the $T = 300$ K, the most prominent effects of temperature on the Ω_1^{st} occur in the LCS3a and LCS3b for $R/h = 20$ with different models, while those influences occur in LCS3b for $R/h = 50$, at $T = 700$ K. For instance, at $R/h = 20$, the most pronounced influences of temperature on the critical axial load occur in the U and X models of LCS3a, are (− 24.7%) and (− 27.1%), respectively, while those influences are (− 24.5%) and (− 23.1%) occur in the V and ◊ models, at $R/h = 50$ (see Fig. 9).

In Tables 11 and 12, the variation of N_{1ax}^{crst}, N_{1ax}^{crkl} and corresponding circumferential wave numbers (n_{cr}) for laminated cylindrical shells with seven different alignments consisting of U, V, ◊ and X model-plies against the $V_{cn}^{*(k)}$ considering $T = 300,\ 500,\ 700$ K, $R/h = 20,\ L/R = 1$ within shear deformation and Kirchhoff–Love theories are examined. In the SDT and KLT frame, the values of the N_{1ax}^{cr} for shells consisting of U, V, ◊ and X patterned plies increases regularly as $V_{cn}^{*(k)}$ rises. When we examine each ply within itself in the framework of SDT, we see that the largest values of N_{1ax}^{crst} in U, V, ◊ and X patterned shells at every value of $V_{cn}^{*(k)}$ is generally in the X patterned shell. There are some exceptional cases. For example, the largest N_{1ax}^{crst} values in LCS2 and LCS4a is in the U pattern shell. When we examine each laminated shell in the SDT framework, the lowest critical axial load values in U, V, ◊ and X patterned shells at all three values of $V_{cn}^{*(k)}$ is seen in the shell consisting of ◊ patterned layers. When each ply is compared within itself at all three values of $V_{cn}^{*(k)}$ in the SDT frame, the lowest circumferential wave numbers corresponding to the critical axial loads generally do not change in the U, V, ◊ and X patterned shells.

As the temperature increases, the influence of the models on the critical axial load increases significantly, and the unique effects of the models maintain their importance. When the critical axial load values of various patterned, aligned and layered cylindrical shells are evaluated together at $T = 300$, 500 and 700 K; in the V-patterned shell with the LCS4c sequence, the most prominent model effect on the N_{1ax}^{crst} occurs at $V_{cn}^{*(k)} = 0.28$ with (− 21.7%), (− 23.7%) and (− 24.8%), respectively, while the weakest V model influence emerges in the LCS2 at $V_{cn}^{*(k)} = 0.12$ with (− 0.34%), (− 0.21%) and (− 1.4%) at $T = 300$, 500 and 700 K, respectively. In the shell with that pattern ◊ and LCS4c arrangement, the prominent influence of the ◊ model on N_{1ax}^{crst} occurs at $V_{cn}^{*(k)} = 0.12$ (− 26.9%, − 28.1%, − 28.4%), respectively, while the least effect occurs in the shell with LCS2 arrangement, at $V_{cn}^{*(k)} = 0.17$ (− 10.1%, − 11.2%, − 4.5%), respectively. The most significant effect of the X model on the N_{1ax}^{crst} occurs at $V_{cn}^{*(k)} = 0.17$ (+ 20.2%, + 19.6%, + 17.2%) in the shell with the LCS4c sequence, while the least effect occurs at $V_{cn}^{*(k)} = 0.28$ (− 0.94%, − 2.3%, − 1.8%) in the shell with the LCS4c sequence, at $T = 300$, 500 and 700 K, respectively.

As the temperature increases, the effect of shear deformations on the critical axial load increases significantly, and the model effects maintain their distinctness and importance. The most prominent shear strains effects on the N_{1ax}^{crst} emerge at $V_{cn}^{*(k)} = 0.28$ with (+ 20.7%, + 25.9%, + 36.5%), (+ 11.3%, + 14.2%, + 21.2%), (+ 8%, + 10.4%, + 16.9%) and (+ 32.1%, + 39.3%, + 51%), respectively, in the U, V, ◊ and X-model LCS3a, at $T = 300$, 500 and 700 K. The weakest shear strains effect on N_{1ax}^{crst} emerges in the LCS3a at $V_{cn}^{*(k)} = 0.12$ with (+ 1.63%) among all models, at $T = 300$ K. As T increases, the weak effect of shear deformations increases to around 2.2%. In addition, the effect of shear strains in three layered shells starting from (0°) is more evident than the effect in three layered shells starting with (90°). Likewise, the shear strains effect in four-layer shells

starting with (0°) is more evident than those effect in four-layer shells starting with (90°). While the effect of the layer arrangement on the critical axial load increases with the rise of the temperature, the influences of models maintain their importance. At $T = 300$ K, the most prominent alignment effects on the N_{1ax}^{crst} occur at $V_{cn}^{*(k)} = 0.28$ with (− 35.4%), (− 25%), (− 19.1%) and (− 48.3%), respectively, in the U, V, ◊ and X-model shells with 0/90 arrangement. At $T = 700$ K, the most prominent alignment effects on the N_{1ax}^{crst} occur at $V_{cn}^{*(k)} = 0.28$ with (− %39.3), (− %31.5), (− %30.4) and (− %52.1), respectively, in the U, V, ◊ and X-model shells with LCS2 arrangement. The alignment effects in percentage for $T = 500$ K vary between the percentage of the alignment influences at $T = 300$ and 700 K.

In Tables 13 and 14, the variation of the values of dimensionless frequency parameter and corresponding wave numbers for laminated cylindrical shells consisting of nanocomposite-plies against the $V_{cn}^{*(k)}$ considering $T = 300,\ 500,\ 700$ K, $R/h = 20$, $L/R = 1$ within SDT and KLT are evaluated. In the SDT and KLT frame, the values of the Ω_1 for shells consisting of U, V, ◊ and X patterned layers increases regularly as $V_{cn}^{*(k)}$ increment. When we examine each ply within itself in the framework of SDT, we see that the largest values of Ω_1^{st} in U, V, ◊ and X model shells at every value of $V_{cn}^{*(k)}$ is generally in the X model shell. There are some exceptional cases. For example, the largest Ω_1^{st} values in LCS2 and LCS3a plies emerges in the U model shell. The lowest dimensionless frequency parameter values in U, V, ◊ and X model shells at $V_{cn}^{*(k)} = 0.14$, 0.17 and 0.28 occurs in the shell consisting of ◊ model plies within SDT. When each layer is compared within itself at $V_{cn}^{*(k)} = 0.14$, 0.17 and 0.28, the lowest wave numbers corresponding to the values of Ω_1^{st} generally do not change in the U, V, ◊ and X model shells. As the temperature increases, the influence of the models on the Ω_1^{st} increases more slowly compared to the critical axial load, and difference between the unique effects of the models reduces. When the values of Ω_1^{st} for various patterned, aligned and laminated cylindrical shells are evaluated together at $T = 300$, 500 and 700 K the most prominent influences of models on the Ω_1^{st} emerge in LCS4b at $V_{cn}^{*(k)} = 0.28$ and weakest V model effect occurs in the LCS2 at $V_{cn}^{*(k)} = 0.12$. As the temperature increases, the effect of shear deformations on the frequency parameter increases, and the model effects maintain their distinctness and importance. The most prominent shear strains effects on the Ω_1^{st} occur at $V_{cn}^{*(k)} = 0.28$ in the LCS3a consisting of the U, V, ◊ and X-models with (+ 10.9%, + 13. 9%, + 20.3%), (+ 5.8%, + 7.4%, + 11.2%), (+ 4.1%, + 5.4%, + 8.8%) and (+ 17.6%, + 22.1%, + 30%), respectively, as $T = 300$, 500 and 700 K. The weakest effect on Ω_1^{st} emerges in the cylindrical shell with the LCS2 alignment with (+ 0.66%) among all models, at $V_{cn}^{*(k)} = 0.17$ and $T = 300$ K. As T increases, the weak effect of shear strains rises to around 1.3%.

The influence of sequences on the Ω_1^{st} increases significantly, and the model effects maintain their distinctness and importance, at the temperature increases. The most prominent sequence effects on the Ω_1^{st} occur in the shells with LCS2 arrangement at $V_{cn}^{*(k)} = 0.28$. For example, the most prominent sequence influences on the Ω_1^{st} are (− %19.6), (− %13.4), (− %10) and (− %28) for U, V, ◊ and X-model, respectively, at $T = 300$ K, while those effects are (− %22.1), (− %17.2), (− %16.6) and (− %32.6), respectively, at $T = 700$ K. For $T = 500$ K, the sequence effects on Ω_1^{st} in percentage terms are larger than those at $T = 300$ K and smaller than those at 700 K.

6 Conclusions

In this study, effective findings are presented regarding the vibration and stability behaviors of laminated cylindrical shells formed by nanocomposite plies under axial load in thermal environments. Each layer of the laminated cylindrical shell has the same volume fraction of CNT and forming a piecewise continuous functionally graded model ply. The extended Voight micromechanical model is used to determine orthotropic and temperature-dependent material properties of laminated nanocomposite cylindrical shells. The dynamic stability equations derived within extended SDT are solved by applying the Galerkin procedure. Finally, the influences of various independent factors, such as the number and sequence of plies, functionally graded models, shear strains, thermal environment, on the non-dimensional critical axial load and non-dimensional frequency parameter of laminated nanocomposite cylindrical shells under axial load are analyzed and interpreted.

Author contributions I am the sole author. A.H.S. contributed to the conceptualization, methodology, software, validation, formal analysis, investigation, resources, writing—original draft preparation, and writing—review and editing.

Funding Open access funding provided by the Scientific and Technological Research Council of Türkiye (TÜBİTAK). This article received no funding support.

Data availability No data were reported in this study.

Declarations

Conflict of interest The authors declare that they have no competing interest.

Informed consent Not applicable.

Institutional review board statement Not applicable.

Appendix A

L_{ij} $(i,\ j = 1,\ 2,\ ...,\ 4)$ are defined by

$$
\begin{aligned}
&L_{11} = h\frac{\partial^2}{\partial x^2}\left[(i_{11}-i_{31})\frac{\partial^2}{\partial y^2} + i_{12}\frac{\partial^2}{\partial x^2}\right],\ \ L_{12} = -\frac{\partial^2}{\partial x^2}\left[i_{13}\frac{\partial^2}{\partial x^2} + (i_{14}+i_{32})\frac{\partial^2}{\partial y^2}\right],\\
&L_{13} = \frac{\partial}{\partial x}\left[i_{15}\frac{\partial^2}{\partial x^2} + i_{35}\frac{\partial^2}{\partial y^2} - \Lambda_3\right],\ \ L_{14} = (i_{18}+i_{38})\frac{\partial^3}{\partial x^2\partial y}, L_{21} = h\frac{\partial^2}{\partial y^2}\left[i_{21}\frac{\partial^2}{\partial y^2} + (i_{22}-i_{31})\frac{\partial^2}{\partial x^2}\right],\\
&L_{22} = -\frac{\partial^2}{\partial y^2}\left[(i_{32}+i_{23})\frac{\partial^2}{\partial x^2} + i_{24}\frac{\partial^2}{\partial y^2}\right],\ L_{23} = (i_{35}+i_{25})\frac{\partial^3}{\partial x\partial y^2},\ \ L_{24} = \frac{\partial}{\partial y}\left(i_{38}\frac{\partial^2}{\partial x^2} + i_{28}\frac{\partial^2}{\partial y^2} - \Lambda_4\right)\\
&L_{31} = h\left[j_{11}\frac{\partial^4}{\partial y^4} + (j_{12}+j_{21}+j_{31})\frac{\partial^4}{\partial x^2\partial y^2} + j_{22}\frac{\partial^4}{\partial x^4}\right],\\
&L_{32} = \frac{1}{R}\frac{\partial^2}{\partial x^2} - j_{23}\frac{\partial^4}{\partial x^4} - (j_{24}+j_{13}-j_{32})\frac{\partial^4}{\partial x^2\partial y^2} - j_{14}\frac{\partial^4}{\partial y^4},\\
&L_{33} = \frac{\partial}{\partial x}\left[j_{25}\frac{\partial^2}{\partial x^2} + (j_{15}+j_{35})\frac{\partial^2}{\partial y^2}\right],\ \ L_{34} = \frac{\partial}{\partial y}\left[(j_{28}+j_{38})\frac{\partial^2}{\partial x^2} + j_{18}\frac{\partial^2}{\partial y^2}\right],\\
&L_{41} = \frac{h}{R}\frac{\partial^2}{\partial x^2},\ \ L_{42} = -N_{ax}\frac{\partial^2}{\partial x^2} - \rho_1\frac{\partial^2}{\partial t^2},\ L_{43} = \Lambda_3\frac{\partial}{\partial x},\ \ L_{44} = \Lambda_4\frac{\partial}{\partial y}.
\end{aligned}
\tag{A1}
$$

where

$$
\begin{aligned}
&i_{11}=A^1_{11}j_{11}+A^1_{12}j_{21},\ i_{12}=A^1_{11}j_{12}+A^1_{12}j_{22},\ i_{13}=A^1_{11}j_{13}+A^1_{12}j_{23}+A^2_{11}, i_{14}=A^1_{11}j_{14}+A^1_{12}j_{24}+A^2_{12},\\
&i_{15}=A^1_{11}j_{15}+A^1_{12}j_{25}+A^1_{15}, i_{18}=A^1_{11}j_{18}+A^1_{12}j_{28}+A^1_{18}, i_{21}=A^1_{21}j_{11}+A^1_{22}j_{21},\ i_{22}=A^1_{21}j_{12}+A^1_{22}j_{22},\\
&i_{23}=A^1_{21}j_{13}+A^1_{22}j_{23}+A^2_{21}, i_{24}=A^1_{21}j_{14}+A^1_{22}j_{24}+A^2_{22},\ i_{25}=A^1_{21}j_{15}+A^1_{22}j_{25}+A^1_{25},\\
&i_{28}=A^1_{21}j_{18}+A^1_{22}j_{28}+A^1_{28},\ i_{31}=A^1_{66}j_{31},\ i_{32}=A^1_{66}j_{32}+2A^2_{66},\ i_{35}=A^1_{35}-A^1_{66}j_{35},\ i_{38}=A^1_{38}-A^1_{66}j_{38},\\
&j_{11}=\frac{A^0_{22}}{\overline{A}},\ j_{12}=-\frac{A^0_{12}}{\overline{A}},\ j_{13}=\frac{A^0_{12}A^1_{21}-A^1_{11}A^0_{22}}{\overline{A}},\ j_{14}=\frac{A^0_{12}A^1_{22}-A^1_{12}A^0_{22}}{\overline{A}},\ j_{15}=\frac{A^0_{25}A^0_{12}-A^0_{15}A^0_{22}}{\overline{A}},\\
&j_{18}=\frac{A^0_{28}A^0_{12}-A^0_{18}A^0_{22}}{\overline{A}},\ j_{21}=-\frac{A^0_{21}}{\overline{A}},\ j_{22}=\frac{A^0_{11}}{\overline{A}},\ j_{23}=\frac{A^1_{11}A^0_{21}-A^1_{21}A^0_{11}}{\overline{A}},\ j_{24}=\frac{A^1_{12}A^0_{21}-A^1_{22}A^0_{11}}{\overline{A}},\\
&j_{25}=\frac{A^0_{15}A^0_{21}-A^0_{25}A^0_{11}}{\overline{A}},\ j_{28}=\frac{A^0_{18}A^0_{21}-A^0_{28}A^0_{11}}{\overline{A}},\ j_{31}=\frac{1}{A^0_{66}},\ j_{32}=-\frac{2A^1_{66}}{A^0_{66}},\ j_{35}=\frac{A^0_{35}}{A^0_{66}},\ j_{38}=\frac{A^0_{38}}{A^0_{66}},\\
&\overline{A}=A^0_{11}A^0_{22}-A^0_{12}A^0_{21},\ \Lambda_q=\sum_{k=1}^{N}\Big[f^{(k)}(z_k)-f^{(k)}(z_{k-1})\Big],(q=3,4).
\end{aligned}
\tag{A2}
$$

in which

$$
\begin{aligned}
&A^{k_1}_{11}=\sum_{k=1}^{N}\int_{z_{k-1}}^{z_k}Q^{(k)}_{11(z_1,T)}z^{k_1}\mathrm{d}z,\ A^{k_1}_{12}=\sum_{k=1}^{N}\int_{z_{k-1}}^{z_k}Q^{(k)}_{12(z_1,T)}z^{k_1}\mathrm{d}z,\ =\sum_{k=1}^{N}\int_{z_{k-1}}^{z_k}Q^{(k)}_{21(z_1,T)}z^{k_1}\mathrm{d}z=A^{k_1}_{21}, A^{k_1}_{22}=\sum_{k=1}^{N}\int_{z_{k-1}}^{z_k}Q^{(k)}_{22(z_1,T)}z^{k_1}\mathrm{d}z,\\
&A^{k_1}_{66}=\sum_{k=1}^{N}\int_{z_{k-1}}^{z_k}Q^{(k)}_{66(z_1,T)}z^{k_1}\mathrm{d}z,\ A^{k_2}_{15}=\sum_{k=1}^{N}\int_{z_{k-1}}^{z_k}Q^{(k)}_{11(z_1,T)}\Lambda^{(k)}_{1(z,T)}z^{k_2}\mathrm{d}z,\ A^{k_2}_{18}=\sum_{k=1}^{N}\int_{z_{k-1}}^{z_k}Q^{(k)}_{12(z_1,T)}\Lambda^{(k)}_{2(z,T)}z^{k_2}\mathrm{d}z,\\
&A^{k_2}_{25}=\sum_{k=1}^{N}\int_{z_{k-1}}^{z_k}Q^{(k)}_{21(z_1,T)}\Lambda^{(k)}_{1(z,T)}z^{k_2}\mathrm{d}z,\ A^{i_2}_{28}=\sum_{k=1}^{N}\int_{z_{k-1}}^{z_k}Q^{(k)}_{22(z_1,T)}\Lambda^{(k)}_{2(z,T)}z^{k_2}\mathrm{d}z,\ A^{i_2}_{35}=\sum_{k=1}^{N}\int_{z_{k-1}}^{z_k}Q^{(k)}_{66(z_1,T)}\Lambda^{(k)}_{1(z,T)}z^{k_2}\mathrm{d}z,\\
&A^{k_2}_{38}=\sum_{k=1}^{N}\int_{z_{k-1}}^{z_k}Q^{(k)}_{66(z_1,T)}\Lambda^{(k)}_{2(z,T)}z^{k_2}\mathrm{d}z,\ k_1=0,\,1,\,2;\ k_2=0,1.
\end{aligned}
\tag{A3}
$$

Appendix B

S_{ij} are given by,

$$
\begin{aligned}
&S_{11}=h\Big[(i_{11}-i_{31})\Big(\frac{n}{R}\Big)^2+i_{12}\Big(\frac{m\pi}{L}\Big)^2\Big]\Big(\frac{m\pi}{L}\Big)^2,\ S_{12}=\Big[(i_{14}+i_{32})\Big(\frac{n}{R}\Big)^2+i_{13}\Big(\frac{m\pi}{L}\Big)^2\Big]\Big(\frac{m\pi}{L}\Big)^2\\
&S_{13}=\Big[i_{15}\Big(\frac{m\pi}{L}\Big)^2+i_{35}\Big(\frac{n}{R}\Big)^2+\Lambda_3\Big]\frac{m\pi}{a},\ S_{14}=(i_{18}+i_{38})\frac{n}{R}\Big(\frac{m\pi}{L}\Big)^2,\\
&S_{21}=h\Big[i_{21}\Big(\frac{n}{R}\Big)^2+(i_{22}-i_{31})\Big(\frac{m\pi}{L}\Big)^2\Big]\Big(\frac{n}{R}\Big)^2,\ S_{22}=\Big[(i_{32}+i_{23})\Big(\frac{m\pi}{L}\Big)^2+i_{24}\Big(\frac{n}{R}\Big)^2\Big]\Big(\frac{n}{R}\Big)^2,\\
&S_{23}=(i_{25}+i_{35})\Big(\frac{m\pi}{L}\Big)\Big(\frac{n}{R}\Big)^2,\ S_{24}=\Big[i_{28}\Big(\frac{n}{R}\Big)^2+i_{38}\Big(\frac{m\pi}{L}\Big)^2+\Lambda_4\Big]\frac{n}{R},\\
&S_{31}=h\Big[j_{22}\Big(\frac{m\pi}{L}\Big)^4+(j_{12}+j_{21}+j_{31})\Big(\frac{mn\pi}{LR}\Big)^2+j_{11}\Big(\frac{n}{R}\Big)^4\Big],\\
&S_{32}=j_{23}\Big(\frac{m\pi}{L}\Big)^4+(j_{24}+j_{13}+j_{32})\Big(\frac{mn\pi}{LR}\Big)^2+j_{14}\Big(\frac{n}{R}\Big)^4+\frac{1}{R}\Big(\frac{m\pi}{L}\Big)^2,\\
&S_{33}=\Big[j_{25}\Big(\frac{m\pi}{L}\Big)^2+(j_{15}+j_{35})\Big(\frac{n}{R}\Big)^2\Big]\frac{m\pi}{L},\ S_{34}=\Big[(j_{28}+j_{38})\Big(\frac{m\pi}{L}\Big)^2+j_{18}\Big(\frac{n}{R}\Big)^2\Big]\frac{n}{R},\\
&S_{41}=\frac{h}{R}\Big(\frac{m\pi}{L}\Big)^2,\ S_{42}=-N_{ax}\Big(\frac{m\pi}{L}\Big)^2-\Omega^2\rho_1,\ \ S_{43}=\Lambda_3\frac{m\pi}{L},\ \ S_{44}=\Lambda_4\frac{n}{R}.
\end{aligned}
\tag{B1}
$$

References

1. Harris, P.J.F.: Carbon nanotubes and related structures, new materials for the twenty-first century. Cambridge University Press, UK (2000). https://doi.org/10.1119/1.1645289
2. Journet, C., Maser, W.K., Bernier, P., Loiseau, A., Lamy de la Chapelle, M., Lefrant, A., Deniard, P., Lee, R., Fischer, J.E.: Large-scale production of single-walled carbon nanotubes by the electric-arc technique. Nature **388**, 756–758 (1997)
3. Rinzler, A.G., Liu, J., Dai, H., Nikolaev, P., Huffman, C.B., Todriguez-Macias, F.J., Boul, P.J., Lu, A.H., Heymann, D., Colbert, D.T., Lee, R.S., Fischer, J.E., Rao, A.M., Eklund, P.C., Smalley, R.E.: Large-scale purification of single-wall carbon nanotubes: process, product, and characterization. Appl. Phys. A **67**, 29–37 (1998). https://doi.org/10.1007/s003390050734
4. Natsuki, T., Tantrakarn, K., Endo, M.: Prediction of elastic properties for single-walled carbon nanotubes. Carbon **42**, 39–45 (2004). https://doi.org/10.1016/j.carbon.2003.09.011
5. Valavala, P.K., Odegard, G.M.: Modeling techniques for determination of mechanical properties of polymer nanocomposites. Rev. Adv. Mater. Sci. **9**, 34–44 (2005)
6. Han, Y., Elliott, J.: Molecular dynamics simulations of the elastic properties of polymer/carbon nanotube composites. Comput. Mater. Sci. **39**, 315–323 (2007). https://doi.org/10.1016/j.commatsci.2006.06.011
7. Gupta, A.K., Harsha, S.P.: Analysis of mechanical properties of carbon nanotubes reinforced polymer composites using multi-scale finite element modelling. Compos. B Eng. **95**, 172–178 (2016). https://doi.org/10.1016/j.compositesb.2016.04.005
8. Lau, K.T., Hui, D.: The revolutionary creation of new advanced materials-carbon nanotube composites. Compos. Part B **33**, 263–277 (2002). https://doi.org/10.1016/S1359-8368(02)00012-4
9. Files, B.S.: Processing of carbon nanotubes for revolutionary space applications. pp. 2000–5345. AIAA (2000). https://doi.org/10.2514/6.2000-5345
10. Shen, H.-S., Xiang, Y.: Torsional postbuckling behavior of FG-GRC laminated cylindrical shells in thermal environments. Thin-Wall. Struct. **135**, 560–574 (2019). https://doi.org/10.1016/j.tws.2018.11.025
11. Shen, H.-S., Xiang, Y.: Postbuckling behavior of functionally graded graphene-reinforced composite laminated cylindrical shells under axial compression in thermal environments. Computer Meth. Appl. Mech. Eng. **330**, 64–82 (2018). https://doi.org/10.1016/j.ijmecsci.2017.11.031
12. Shen, H.-S., Xiang, Y.: Thermal buckling and postbuckling behavior of FG-GRC laminated cylindrical shells with temperature-dependent material properties. Meccanica **54**(1–2), 283–297 (2019). https://doi.org/10.1007/s11012-019-00945-0
13. Shen, H.-S., Xiang, Y., Fan, Y.: Postbuckling of functionally graded graphene-reinforced composite laminated cylindrical panels under axial compression in thermal environments. Int. J. Mech. Sci. **135**, 398–409 (2018). https://doi.org/10.1016/j.ijmecsci.2017.11.031
14. Hoang, V.N.V., Tien, N.D., Ninh, D.G., Thang, V.T., V.T., DV Truong, D.V.: Nonlinear dynamics of functionally graded graphene nanoplatelet reinforced polymer doubly-curved shallow shells resting on elastic foundation using a micromechanical model. J. Sand. Struct. Mater. **23**(7), 3250–3279 (2021). https://doi.org/10.1177/1099636220926650
15. Hoang, V.N.V., Ninh, D.G., Bao, H.V., Huy, V.L.: Behaviors of dynamics and stability standard of graphene nanoplatelet reinforced polymer corrugated plates resting on the nonlinear elastic foundations. Compos. Struct. **260**, 113253 (2021). https://doi.org/10.1016/j.compstruct.2020.113253
16. Tien, N.D., Hoang, V.N.V., Ninh, D.G., Huy, V.L., Hung, N.C.: Nonlinear dynamics and chaos of a nanocomposite plate subjected to electro–thermo–mechanical loads using Flügge–Lur'e–Bryrne theory. J. Vib. Control **27**(9–10), 1184–1197 (2021). https://doi.org/10.1177/1077546320938
17. Ninh, D.G., Quan, N.M., Hoang, V.N.V.: Thermally vibrational analyses of functionally graded graphene nanoplatelets reinforced funnel shells with different complex shapes surrounded by elastic foundation. Mech. Adv. Mater. Struct. **29**(26), 4654–4676 (2022). https://doi.org/10.1080/15376494.2021.1934763
18. Lei, Z.X., Zhang, L.W., Liew, K.M.: Free vibration analysis of laminated FG-CNT reinforced composite rectangular plates using the kp-Ritz method. Compos. Struct. **127**, 245–259 (2015). https://doi.org/10.1016/j.compstruct.2015.03.019
19. Lei, Z.X., Zhang, L.W., Liew, K.M.: Parametric analysis of frequency of rotating laminated CNT reinforced functionally graded cylindrical panels. Compos. Part B Eng. **90**, 251–266 (2016). https://doi.org/10.1016/j.compositesb.2015.12.024
20. Chiker, Y., Bachene, M., Bouaziz, S., Guemana, M., Ben Amar, M., Haddar, M.: Free vibration analysis of hybrid laminated plates containing multilayer functionally graded carbon nanotube-reinforced composite plies using a layer-wise formulation. Arch. Appl. Mech. **91**(1), 463–485 (2021). https://doi.org/10.1007/s00419-020-01783-3
21. Nguyen, P.D., Papazafeiropoulos, G., Vu, Q.V., Duc, N.D.: Buckling response of laminated FG-CNT reinforced composite plates: analytical and finite element approach. Aerosp. Sci. Technol. **121**, 107368 (2022). https://doi.org/10.1016/j.ast.2022.107368
22. Chakraborty, S., Dey, T., Kumar, R.: Stability and vibration analysis of CNT-reinforced functionally graded laminated composite cylindrical shell panels using semi-analytical approach. Compos. Part B Eng. **168**, 1–14 (2019). https://doi.org/10.1016/j.compositesb.2018.12.051
23. Avey, M., Fantuzzi, N., Sofiyev, A.H.: Vibration of laminated functionally graded nanocomposite structures considering the transverse shear stresses and rotary inertia. Compos. Struct. **301**, 116209 (2022). https://doi.org/10.1016/j.compstruct.2022.116209
24. Avey, M., Fantuzzi, N., Sofiyev, A.H.: On the solution of thermal buckling problem of moderately thick laminated conical shells containing carbon nanotube originating layers. Materials **15**(21), 7427 (2022). https://doi.org/10.3390/ma15217427
25. Shen, H.-S., Li, C., Huang, X.H.: Assessment of negative Poisson's ratio effect on the postbuckling of pressure-loaded FG-CNTRC laminated cylindrical shells. Mech. Bas. Des. Struct. Mach. **51**(4), 1856–1880 (2023). https://doi.org/10.1080/15397734.2021.1880934
26. Shen, H.-S.: Postbuckling Behavior of Plates and Shells. World Scientific Publishing Co. Pte. Ltd., Singapore (2017). https://doi.org/10.1142/10208
27. Volmir, A.S.: Stability of Elastic Systems. Nauka, Moscow, Russia (1967)

28. Ambartsumyan, S.A.: Theory of Anisotropic Shells. NASA, TT F–118, (1964)
29. Reddy, J.N.: Mechanics of Laminated Composite Plates and Shells. Theory and Analysis. CRC Press, New York (2004). https://doi.org/10.1201/b12409
30. Seidel, G.D., Lagoudas, D.C.: Micromechanical analysis of the effective elastic properties of carbon nanotube reinforced composites. Mech. Mater. **38**, 884–907 (2006). https://doi.org/10.1016/j.mechmat.2005.06.029
31. Anumandla, V., Gibson, R.F.: A comprehensive closed form micromechanics model for estimating the elastic modulus of nanotube-reinforced composites. Compos. A Appl. Sci. **37**, 2178–2185 (2006). https://doi.org/10.1016/j.compositesa.2005.09.016
32. Li, X., Gao, H., Scrivens, W.A., Fei, D., Xu, X., Sutton, M.A., Reynolds, P., Myrick, M.L.: Reinforcing mechanisms of single-walled carbon nanotube-reinforced polymer composites. J. Nanosci. Nanotechnol. **7**, 2309–2317 (2007). https://doi.org/10.1166/jnn.2007.410
33. Esawi, A.M.K., Farag, M.M.: Carbon nanotube reinforced composites: potential and current challenges. Mater. Des. **28**, 2394–2401 (2007). https://doi.org/10.1016/j.matdes.2006.09.022
34. Formica, G., Lacarbonara, W., Alessi, R.: Vibrations of carbon nanotube-reinforced composites. J. Sound Vib. **329**, 1875–1889 (2010). https://doi.org/10.1016/j.jsv.2009.11.020
35. Wang, J., Pyrz, R.: Prediction of the overall moduli of layered silicate-reinforced nanocomposites-part I: Basic theory and formulas. Compos. Sci. Technol. **64**, 925–934 (2004). https://doi.org/10.1016/S0266-3538(03)00024-1
36. Shen, H.-S.: Postbuckling of nanotube-reinforced composite cylindrical shells in thermal environments, Part I: Axially-loaded shells. Compos. Struct. **93**, 2096–2108 (2011). https://doi.org/10.1016/j.compstruct.2011.04.005
37. Shen, H.-S., Xiang, Y.: Nonlinear vibration of nanotube-reinforced composite cylindrical shells in thermal environments. Comput. Methods Appl. Mech. Eng. **213**, 196–205 (2012). https://doi.org/10.1016/j.cma.2011.11.025
38. Fazzolari, F.A.: Thermoelastic vibration and stability of temperature-dependent carbon nanotube-reinforced composite plates. Compos. Struct. **196**, 199–214 (2018). https://doi.org/10.1016/j.compstruct.2018.04.026
39. Fazzolari, F.A.: Elastic buckling and vibration analysis of FG polymer composite plates embedding graphene nanoplatelet reinforcements in thermal environment. Mech. Adv. Mater. Struct. **28**(4), 391–404 (2021). https://doi.org/10.1080/15376494.2019.1567886